A&A 641, A43 (2020)
https://doi.org/10.1051/0004-6361/202038682

Astronomy & Astrophysics

Is HR 6819 a triple system containing a black hole?

An alternative explanation*

J. Bodensteiner, T. Shenar, L. Mahy, M. Fabry, P. Marchant, M. Abdul-Masih, G. Banyard, D. M. Bowman, K. Dsilva, A. J. Frost, C. Hawcroft, M. Reggiani, and H. Sana

Institute of Astronomy, KU Leuven, Celestijnenlaan 200D, 3001 Leuven, Belgium
e-mail: julia.bodensteiner@kuleuven.be

Received 17 June 2020 / Accepted 16 July 2020

ABSTRACT

Context. HR 6819 was recently proposed to be a triple system consisting of an inner B-type giant plus black hole (BH) binary with an orbital period of 40 d and an outer Be tertiary. This interpretation is mainly based on two inferences: that the emission attributed to the outer Be star is stationary and that the inner star, which is used as mass calibrator for the BH, is a B-type giant.
Aims. We re-investigate the properties of HR 6819 to search for a possibly simpler alternative explanation for HR 6819, which does not invoke the presence of a triple system with a BH in the inner binary.
Methods. Based on an orbital analysis, the disentangling of the spectra of the two visible components and the atmosphere analysis of the disentangled spectra, we investigate the configuration of the system and the nature of its components.
Results. Disentangling implies that the Be component is not a static tertiary, but rather a component of the binary in the 40 d orbit. The inferred radial velocity amplitudes of $K_1 = 60.4 \pm 1.0\,\mathrm{km\,s^{-1}}$ for the B-type primary and $K_2 = 4.0 \pm 0.8\,\mathrm{km\,s^{-1}}$ for the Be-type secondary imply an extreme mass ratio of $M_2/M_1 = 15 \pm 3$. We find that the B-type primary, which we estimate to contribute about 45% to the optical flux, has an effective temperature of $T_{\rm eff} = 16 \pm 1$ kK and a surface gravity of $\log g = 2.8 \pm 0.2$ [cgs], while the Be secondary, which contributes about 55% to the optical flux, has $T_{\rm eff} = 20 \pm 2$ kK and $\log g = 4.0 \pm 0.3$ [cgs]. We infer spectroscopic masses of $0.4^{+0.3}_{-0.1}\,M_\odot$ and $6^{+5}_{-3}\,M_\odot$ for the primary and secondary which agree well with the dynamical masses for an inclination of $i = 32°$. This indicates that the primary might be a stripped star rather than a B-type giant. Evolutionary modelling suggests that a possible progenitor system would be a tight ($P_{\rm i} \approx 2$ d) B+B binary system that experienced conservative mass transfer. While the observed nitrogen enrichment of the primary conforms with the predictions of the evolutionary models, we find no indications for the predicted He enrichment.
Conclusions. We suggest that HR 6819 is a binary system consisting of a stripped B-type primary and a rapidly-rotating Be star that formed from a previous mass-transfer event. In the framework of this interpretation, HR 6819 does not contain a BH. Interferometry can distinguish between these two scenarios by providing an independent measurement of the separation between the visible components.

Key words. stars: massive – stars: early-type – stars: emission-line, Be – binaries: close – binaries: spectroscopic

1. Introduction

Massive stars (stars with initial masses $\gtrsim 8\,M_\odot$) have a major impact on their immediate surroundings and the evolution of their entire host galaxies through their energetic radiation, their strong stellar winds, and especially their spectacular explosions (e.g. Jamet et al. 2004; Bromm et al. 2009; Aoki et al. 2014). Yet, a detailed understanding of their formation and complex evolution is still lacking (see e.g. Langer 2012).

One major uncertainty in regards to their evolution is multiplicity. It has been shown observationally that the majority of massive stars are born in binary or higher-order multiple systems (Sana et al. 2012; Kobulnicky et al. 2014; Dunstall et al. 2015; Moe & Di Stefano 2017). A large fraction of these systems interact during their lives, which drastically alters their evolutionary path and the outcome thereof (Paczyński 1967; Podsiadlowski et al. 1992; Vanbeveren & De Loore 1994; de Mink et al. 2013).

Given the high rate of detected gravitational wave events that originate from the merger of two stellar-mass black holes (BHs; Abbott et al. 2019), it is crucial to understand the origin of stellar-mass BHs. Alongside dynamical (Di Carlo et al. 2019; Fragione et al. 2019) as well as primordial (Nishikawa et al. 2019) formation pathways, one of the proposed channels for double-BH formation is close binary evolution (e.g. Belczynski et al. 2002; Mandel & de Mink 2016; Marchant et al. 2016; Abdul-Masih et al. 2019). Focusing on the binary channel, recent theoretical studies predict that a significant fraction of O- and early B-type stars are in binary systems with an unseen BH companion (Langer et al. 2020; Shao & Li 2019; Yi et al. 2019).

While a handful of these can be detected through X-ray emission in so-called high-mass X-ray binaries (HMXBs, see e.g. Liu et al. 2006), a majority of the systems could be X-ray quiet and are thus difficult to detect with observations. This is reflected by the lack of reported OB+BH binaries. Until recently, only a handful of these types of X-ray quiet systems and candidate systems were known. Examples include MWC 656, a Be+BH system (Casares et al. 2014), AS 386, a candidate B[e]+BH binary (Khokhlov et al. 2018), and V Puppis, in which a BH is thought to be the tertiary companion of an eclipsing binary system containing two B-type components (Qian et al. 2008). Thompson et al. (2019) recently proposed that the unseen

* Based on observations made with ESO Telescopes at the La Silla Paranal Observatory under programme ID 63.H-0080 and 073.D-0274.

companion of the rapidly rotating giant star 2MASS J05215658 + 4359220 is a low-mass BH or an unexpectedly massive neutron star. This finding, however, was subsequently challenged by van den Heuvel & Tauris (2020) who propose that the companion could also be a close binary system containing two late-type main sequence stars. Recently, the following two additional systems were proposed to contain a stellar-mass BH: LS V +22 25 (LB-1 hereafter) and HR 6819.

LB-1 was proposed by Liu et al. (2019) to contain a $\approx$70 $M_\odot$ BH in a 79 d orbit with a B-type star companion. This interpretation relied on the adopted mass of the B-type primary and on the apparent low-amplitude motion of the Hα line, which was interpreted to follow the orbit of the unseen secondary. Both these aspects were, however, challenged by subsequent studies. El-Badry & Quataert (2020a) and Abdul-Masih et al. (2020) showed that the anti-phase signature of Hα cannot be readily interpreted as Doppler motion without considering the impact of potential Hα absorption of the B-type component. Simón-Díaz et al. (2020) and Irrgang et al. (2020) performed spectroscopic studies of the primary and found evidence for processed CNO material in its atmosphere, leading Irrgang et al. (2020) to suggest that it is a low-mass stripped helium star. Subsequently, Shenar et al. (2020) utilised spectral disentangling to show that the secondary in LB-1 is not a BH, but a classical Be star – a rapidly rotating B-type star with a decretion disc (see e.g. Rivinius et al. 2013). Shenar et al. (2020) interpreted LB-1 as a post-mass-transfer system (Pols et al. 1991), where the primary was stripped of most of its envelope and the secondary accreted mass and angular momentum to become a Be star. Based on an independent near-infrared study, Liu et al. (2020) recently derived a mass ratio comparable to that reported by Shenar et al. (2020), but remained inconclusive regarding the nature of the secondary. Hence, evidence for the presence of a BH in LB-1 is currently lacking.

The second system that was recently proposed to contain a stellar-mass BH is HR 6819 (Rivinius et al. 2020). It was reported to be variable already by Buscombe & Morris (1960). The composite nature of the spectrum consisting of a narrow-lined component and a broad-line component was reported by Hiltner et al. (1969) and Dachs et al. (1981), who classified the system as B3 IIIep. A similar spectral classification, B3 III(e), was found by Slettebak (1982), who interpreted the star as a "normal sharp-lined B3 giant". Dachs et al. (1986) came to a similar conclusion and retracted their earlier interpretation of a composite spectrum. Based on FEROS data, Maintz (2003) reported an emission profile in Hβ moving in anti-phase with the narrow absorption, proposing that the system might contain a B+Be binary with a 30−60 d period. Wang et al. (2018) studied the system in the UV and did not find any indications for a hot subdwarf companion.

Recently, Rivinius et al. (2020) suggested that HR 6819 hosts the closest stellar-mass BH to the Sun yet reported. They argued that the emission profiles attributed to the rapidly-rotating Be star are stationary on the time scale of years, and that the Be star seen in the spectrum must therefore be a distant tertiary in an outer orbit. Based on the binary mass function ($f_M = 0.96\,M_\odot$) derived from the SB1 RV curve and the mass estimate of the narrow-lined star ($M \geq 5\,M_\odot$), which the authors classified as B3 III, Rivinius et al. (2020) concluded that the unseen secondary star in the 40 d orbit must be more massive than 4 $M_\odot$. Given this mass estimate, they concluded that the unseen companion must be a BH. The system was thus interpreted by Rivinius et al. (2020) as a hierarchical triple containing a B+BH inner binary on a 40 d orbit and a Be star on an unconstrained wider orbit. They suggested a similar configuration for LB-1 which is, however, contradicted by Shenar et al. (2020) and Liu et al. (2020).

In this paper we present an alternative explanation to HR 6819 that does not invoke an inferred stellar-mass BH or a tertiary component on a wider orbit. Our study is based on the same observational data as used by Rivinius et al. (2020), which is described in Sect. 2. In Sect. 3 we derive the orbit of the narrow-lined primary and show additional sources of variability in the composite spectra. In Sect. 4 we describe the disentangling of the spectra while we derive stellar parameters in Sect. 5. To investigate the origin and distribution of emission in the system we apply the Doppler tomography technique in Sect. 6. A possible evolutionary history of the system is discussed in Sect. 7, while the conclusions are given in Sect. 8.

2. Observations and data reduction

Two archival data sets of HR 6819 are available, both obtained with the Fibre-fed Extended Range Optical Spectrograph (FEROS, Kaufer et al. 1999). The first data set, acquired in 1999, contains 12 epochs[1] while the second data set from 2004 contains 51 epochs[2].

Between the two independent data sets, FEROS was moved from the ESO 1.52 m telescope to the 2.2 m MPG/ESO telescope both situated in the La Silla Observatory, Chile. FEROS covers a wavelength range between 3500 and 9200 Åwith a spectral resolving power of 48 000. The journal of observations, including typical signal-to-noise ratios (S/N) and radial velocities (RVs) measured as described in Sect. 3.1 is given in Table A.1.

While observations of the first data set were downloaded fully-reduced, the second data set was reduced using the standard FEROS pipeline (version 1.60). Both include all standard calibrations such as bias and flat-field corrections and wavelength calibrations. A barycentric correction was applied to all spectra. The homogeneity of the wavelength calibration between the two data sets was reviewed using the two interstellar Na I lines at 5890 and 5896 Å. All 63 fully-reduced spectra were individually normalised by fitting a spline to selected anchor points in the continuum of each spectrum.

In addition to the aforementioned FEROS observations, we also consider spectra available in the BeSS[3] database (Neiner et al. 2011). These spectra cover a longer time span (i.e. approximately one observation per year since 2011, see Table A.2), however, their spectral coverage and quality varies. We thus only use them in a qualitative sense in order to investigate variability in the Hα line (see Sect. 3.5).

3. Spectral variability

HR 6819 exhibits spectral variability of the order of days, weeks, and years. The most apparent form of variability is seen through the RV shifts of the narrow-lined primary, which follows a Keplerian orbit of about 40 d. However, other forms of variability, manifested through changes in the line profiles, widths, and depths, are also seen.

[1] Program ID 63.H-0080, available under https://www.lsw.uni-heidelberg.de/projects/instrumentation/Feros/ferosDB/search.html

[2] Program ID 073.D-0274, available on the ESO archive under https://www.eso.org/sci/facilities/lasilla/instruments/feros.html

[3] http://basebe.obspm.fr/basebe/

Table 1. Derived orbital parameters based on our orbital analysis and disentangling, along with their 1σ errors (upper) and estimated physical parameters of the components of HR 6819 based on a spectral analysis with PoWR and TLUSTY (lower).

Parameter	Primary	Secondary
Spectral type	Stripped star	B2-3 Ve
$P_{\rm orb}$ [d]	40.335 ± 0.007	
T_0 [MJD] ($\Phi = 0$)	53116.9 ± 1.1	
e	0 (fixed)	
γ [km s^{-1}]	9.13 ± 0.78	
K [km s^{-1}]	60.4 ± 1.0	4.0 ± 0.8
$M \sin^3 i$ [$M_\odot$]	0.07 ± 0.03	1.05 ± 0.02
$a \sin i$ [$R_\odot$]	48.2 ± 0.8	3.2 ± 0.6
$q(\frac{M_2}{M_1})$	15 ± 3	
$M_{\rm dyn}$ [$M_\odot$]	0.46 ± 0.26	7 ± 2 (fixed)
i [deg]	32 ± 4	
$T_{\rm eff}$ [kK]	16 ± 1	20 ± 2
$\log g$ [cgs]	2.8 ± 0.2	4.0 ± 0.3
Flux $f/f_{\rm tot}(V)$	0.45 (fixed)	0.55 (fixed)
$\log L$ [$L_\odot$]	3.05 ± 0.10	3.35 ± 0.10
R [$R_\odot$]	4.4 ± 0.4	3.9 ± 0.7
$M_{\rm spec}$ [$M_\odot$]	$0.4^{+0.3}_{-0.1}$	6^{+5}_{-3}
$v \sin i$ [km s^{-1}]	$\lesssim 25$	180 ± 10
$v_{\rm eq}$ [km s^{-1}]	$\lesssim 40$	340 ± 40
$v_{\rm macro}$ [km s^{-1}]	35 ± 5	70 ± 25
$v_{\rm micro}$ [km s^{-1}]	10 (fixed)	2 (fixed)

Notes. The luminosity and radii are obtained for an assumed distance of 340 pc (Bailer-Jones et al. 2018).

3.1. Orbital analysis

We measured RVs of the narrow-lined primary star in the combined data set by fitting Gaussian profiles to several spectral lines simultaneously at all observing epochs, based on the method described in Sana et al. (2013). Here, we used several He I and metal lines (i.e. N II, Si II, Si III). We fitted an orbit to the RV data using the python package SPINOS (Fabry et al., in prep.)[4].

We find that the root-mean-square (rms) of the orbit is 4.5 km s^{-1}, which is larger than the typical formal RV errors. Since the formal RV errors are underestimated given the variability in the spectral lines (see Sects. 3.3 and 3.4), we scaled the RV errors by the ratio between the rms and the mean error. The derived eccentricity is consistent with zero within the errors and we thus concluded the orbit to be circular, with ω fixed to 90°. Accordingly, T_0 corresponds to the primary conjunction. Our orbital parameters (see Table 1) agree well with the parameters reported by Rivinius et al. (2020).

3.2. Apparent anti-phase motion of the Hα line

The Hα line in HR 6819 appears to exhibit an anti-phase motion with respect to the primary. This is illustrated in Fig. 1, where two FEROS spectra taken close to quadrature (maximum RV shift) are shown. However, it is not clear without further analysis whether this behaviour is the result of the orbital motion of the Be component, or the superposition of an absorption component in Hα stemming from the narrow-lined primary (Abdul-Masih et al. 2020; El-Badry & Quataert 2020a).

The core of the Hα line remains relatively unchanged. This implies that the narrow-lined primary does not portray

[4] https://github.com/matthiasfabry/spinOS

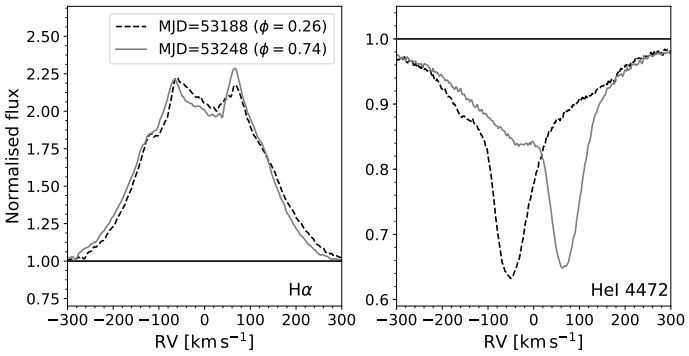

Fig. 1. Two FEROS spectra taken close to quadrature, focusing on the Hα (*left*) and He I λ4472 (*right*) lines. We note the apparent anti-phase motion observed in the Hα line.

significant absorption in Hα. Instead, HR 6819 exhibits a behaviour similar to other Be binaries such as π Aqr (Bjorkman et al. 2002) and o Pup (Koubský et al. 2012), where a trailing emission in Hα is reported to follow the orbit of the low-mass object in the system. The lack of significant absorption in the narrow-lined component may suggest that the apparent anti-phase RV shift observed in Hα is the result of an actual orbital motion of the Be component.

3.3. Short-term variability of He I lines

Significant variability is observed in strong He I lines. Figure 2 shows two FEROS observations of the He I λ4472 and λ5876 lines taken approximately 1 d apart from each other. Very strong variability is apparent in the wings of the He I λ5876 line and, to a lesser extent, the He I λ4472 line. The data appear as if two additional stellar components move rapidly from one side to the other on a very short orbit (i.e. of the order of a day). Such variability can, however, also be explained by non-radial gravity-mode pulsations. This is observed for other Be stars (e.g. Baade 1984; Rivinius et al. 2003; Pápics et al. 2017) and demonstrated by simulations of line profile variability caused by gravity-mode pulsations (Aerts et al. 2009).

We tested the hypothesis of two additional components on an even shorter orbit in the HR 6819 system through multiple-Gaussian fits and period searches. Based on the currently available data, which are typically taken with at least one night in between, we can neither derive a conclusive solution for such a configuration, nor disprove it. In the rest of our analysis, we therefore assume that the system consists of two visible components, and that the variability observed in the strong He I lines is intrinsic to the Be star. This is supported by previous time series spectroscopic studies of Be stars that demonstrate that He I spectral lines are particularly sensitive to intrinsic pulsational variability in moderate and fast-rotating early-B stars (Balona et al. 1999; Rivinius et al. 2003; Aerts et al. 2010). We cannot, however, fully rule out the presence of an inner short-period binary in this 40 d system. Testing this would require securing time-series spectroscopy over the course of one night to sample the short-period (<1 d) variability.

3.4. Medium-term variability of the narrow-lined primary

Significant variability is also observed in the spectrum of the narrow-lined primary. Figure 3 shows three FEROS observations focusing on the Si II $\lambda\lambda$4128, 4131 doublet and the He I λ4472

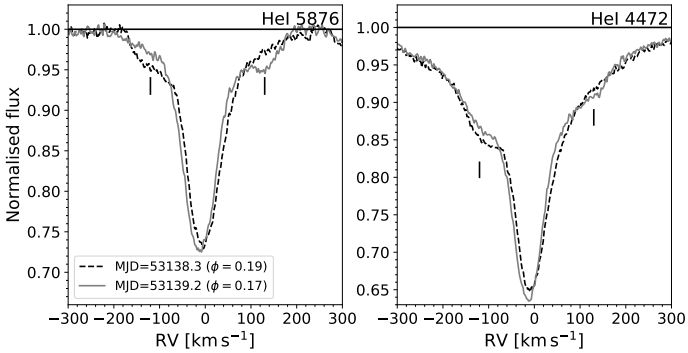

Fig. 2. Two FEROS observations taken on consecutive days, focusing on two He I lines (see legend and labels). We mark the strong variability features seen in the wings of the He I lines.

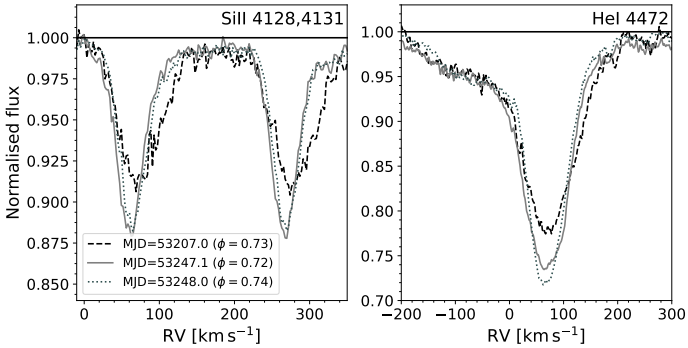

Fig. 3. Three FEROS observations taken at $\phi \approx 0.73$ but at three different days with a time separation of about 1 d and 40 d (see legend). The panels zoom in on two Si II lines, dominated by the narrow-lined primary, and on the He I line, illustrating the apparent variability of the primary's line profiles on the scale of weeks.

line, taken at approximately the same orbital phase, but with relative separations of about 1 d and 40 d. The Si II lines are, as all other metal lines, strongly dominated by the narrow-lined primary. As illustrated in Fig. 3, the line width and depth change significantly over the course of a few weeks, but remain fairly similar over the course of days.

The variability in the Si doublet can also be explained by non-radial gravity-mode pulsations (see Aerts et al. 2009, their Fig. 1) with the silicon doublet (and triplet) being particularly sensitive to pulsations in slowly-rotating stars (Aerts et al. 2009, 2010). Hence, we also interpret this as evidence for non-radial gravity-mode pulsations in the narrow-lined primary. The presence of pulsations is also related to the relatively large macroturbulence derived (see Sect. 5.1.2 Simón-Díaz et al. 2017), since stars with larger pulsation amplitudes typically show larger macroturbulence (Bowman et al. 2020). We also note that Rivinius et al. (2020) demonstrate variability caused by non-radial gravity-mode pulsations using SMEI and TESS photometry, with such low-frequency photometric variability being common among massive stars (Bowman et al. 2019).

3.5. Long-term variability of Balmer lines

Long-term variability in Balmer lines is a common feature of Be stars (Lacy 1977; Rivinius et al. 2013). Different types of variability, probably caused by variations in the disc properties, are known to affect both the shape as well as the strength of the Hα line. In double-peaked emission lines of some Be stars, so-called

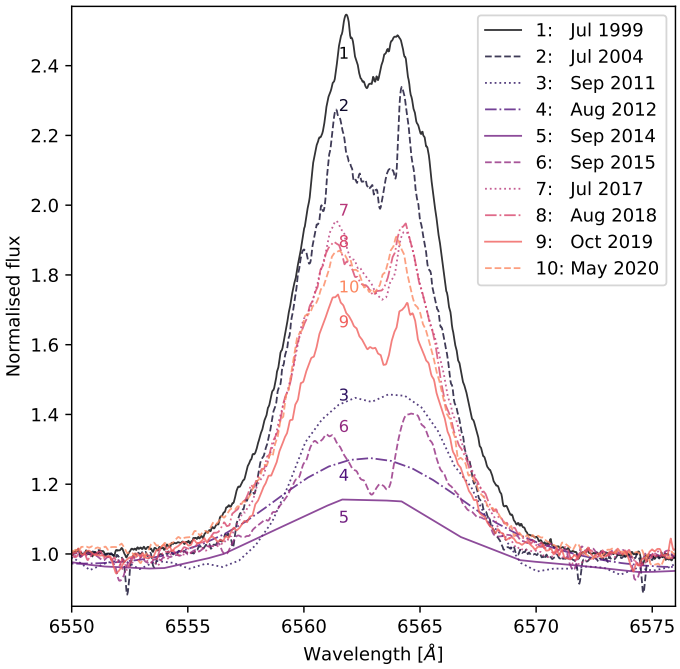

Fig. 4. Evolution of the Hα line in the past 20 years. In addition to the BeSS spectra (more information is given in Table A.2) we plot one spectrum from each FEROS run (i.e. 1999 and 2004, see legend).

violet-to-red (V/R) cycles occur in which the strength of the two emission peaks varies cyclically with respect to each other (Okazaki 1991; Štefl et al. 2009). On the other hand the overall strength of Hα varies on the timescales of years to decades, where the emission can also fully disappear. This probably coincides with the formation and depletion of the circumstellar disc itself (Doazan et al. 1986; Wisniewski et al. 2010; Draper et al. 2011).

We investigated the FEROS and BeSS spectra of HR 6819 that cover different time scales. Figure 4 shows that the strength of the Hα line was highly variable over the past 20 years, while its shape remains rather similar (considering the different resolving powers). The other Balmer lines portray a similar variability, albeit with a much weaker magnitude.

4. Spectral disentangling

We performed spectral disentangling to separate the observed composite spectra into the intrinsic spectra of the stellar components in HR 6819, and to investigate whether they are bound in the 40 d orbit. We used two independent methods, the shift-and-add and the Fourier technique, described below. As implemented here, both disentangling procedures used the SB1 orbital solution of the primary as an input. Having constrained all orbital parameters but K_2, we performed spectral disentangling along the K_2-axis. Specifically, we adopted the orbital parameters derived in Sect. 3.1 and performed multiple disentangling procedures varying K_2 from 0 to 20 km s^{-1} in steps of 0.5 km s^{-1}. In each step we computed the χ^2 of the solution by comparing the disentangled spectra with the observed ones at all available phases.

When disentangling the spectra of HR 6819, we thus implicitly assumed that the Be component participates in the 40 d orbit. If true, our method should retrieve a non-vanishing value for the orbital semi-amplitude K_2. Otherwise, values consistent with

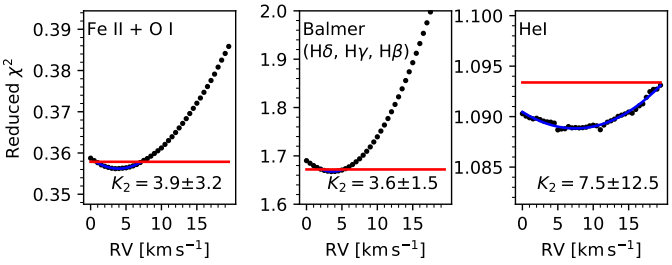

Fig. 5. Reduced $\chi^2(K_2)$ and corresponding K_2 measurements for individual line groups. The red lines depict the 1σ confidence interval.

zero should be obtained, implying that the Be component is a tertiary star.

Owing to the high S/N in the spectra of HR 6819, a multitude of lines can be probed independently. We thus performed disentangling on a series of lines belonging to He I (photospheric absorption), Fe II and O I (disc emission), and Balmer lines (combination of photospheric absorption and disc emission). Given the large variability observed in the Hα line (see Sect. 3.5), we did not consider Hα in our analysis.

Because of the strong variability between the 1999 and 2004 epochs (see Sect. 3.5), we furthermore refrained from combining both data sets. Instead, we focused on the 2004 epoch, for which 51 spectra are available that cover approximately four orbital cycles. A comparison with the 1999 epoch is given in Appendix B.

The shift-and-add technique (e.g. Marchenko et al. 1998; González & Levato 2006; Mahy et al. 2012; Shenar et al. 2018) is an iterative procedure, in which the disentangled spectra calculated in the jth iteration, A_j and B_j, are used to calculate the disentangled spectra for the $j+1$th iteration. To avoid spurious features that are typically observed in the wings of broad lines when using the shift-and-add method (e.g. Marchenko et al. 1998), we forced the solution to be smaller than unity (within the S/N) in regions where it is not expected to exceed unity.

The results of the disentangling using shift-and-add are given in Fig. 5, where we show reduced $\chi^2(K_2)$ and corresponding K_2 measurements for the different line groups used as well as the best-fit. We note that the reduced χ^2 obtained is of the order of unity for all lines considered (see Fig. 5). K_2 measurements of the individual lines are provided in Table C.1. Examples for the fits between individual observations and the disentangled spectra are shown in Fig. 6 for a few lines. A weighted mean of all measurements and their errors yields $K_2 = 4.0 \pm 0.8\,\mathrm{km\,s^{-1}}$. The true error may be larger (e.g. due to pulsational variability), but is difficult to quantify.

We tested these findings by applying the same overall procedure using an independent disentangling technique, namely Fourier disentangling (Ilijić et al. 2004; Hadrava 1995; Ilijić 2017, see Appendix C). Fourier disentangling of the Balmer and Fe II emission lines results in comparable K_2 measurements to those derived using the shift-and-add technique (see Fig. C.1). The He I lines favour values close to zero, but provide little diagnostic power as the 1σ confidence interval is generally larger than $7\,\mathrm{km\,s^{-1}}$. The weighted mean of the measurements and their errors of $3.7 \pm 1.0\,\mathrm{km\,s^{-1}}$ agrees with the shift-and-add method. A detailed comparison to the shift-and-add technique as well as an overview of the K_2 measurements for individual lines is given in Appendix C.

Given the low amplitude derived we further tested both techniques (shift-and-add and Fourier disentangling) using simulated spectra tailor-made for this system (see Appendix C). These

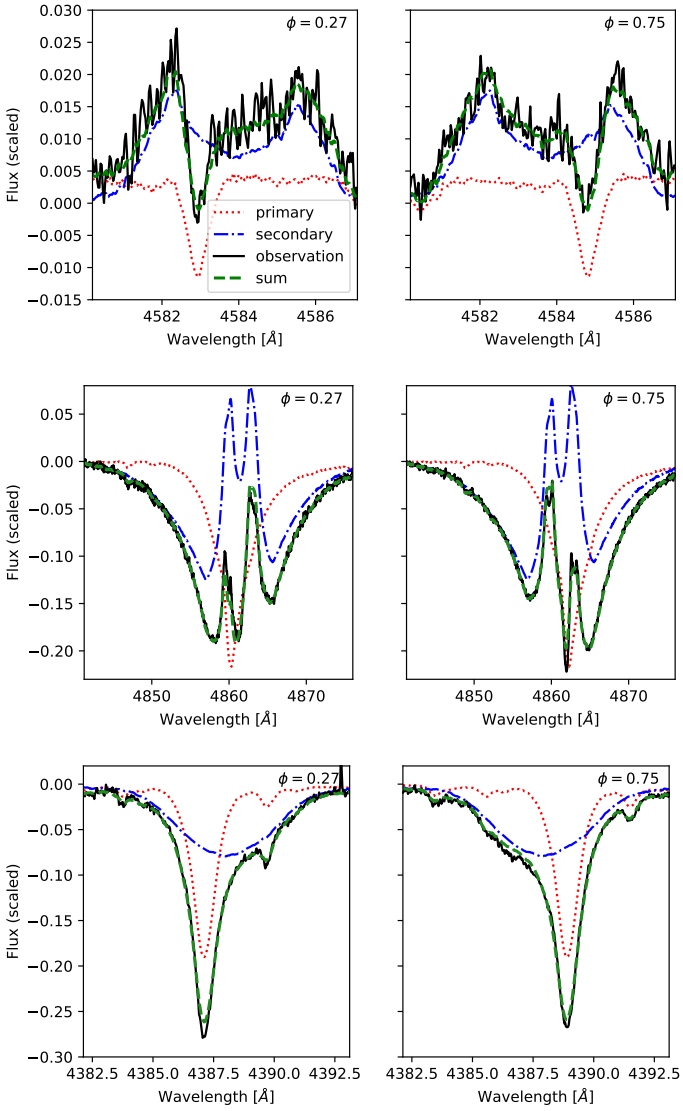

Fig. 6. Illustration of the fit quality between the individual observations at quadrature ($\phi = 0.25$ and 0.75 for the *left* and *right columns*, respectively) and the shift-and-added disentangled spectra. Fits are shown for the Fe II λ4584 line (*top*), Hβ line (*middle*), and He I λ4388 line (*bottom*).

tests show that in general sharp spectral features such as the double-peaked Fe II and Balmer profiles are more sensitive to RV changes in comparison to broad, shallow rotation profiles. We find that both methods successfully retrieve the input parameters of our simulated system when disentangling the Balmer and Fe II lines. In contrast, Fourier disentangling of the He I lines typically yields vanishing K_2 measurements, while the shift-and-add technique generally retrieves the input value. We note that the two disentangling procedures yield similar disentangled spectra. Hence, the spectral analysis (Sect. 5) is unaffected by the choice of method.

Based on this discussion and on the results of Appendix C, we adopt $K_2 = 4.0 \pm 0.8\,\mathrm{km\,s^{-1}}$, implying that the Be component is bound to the narrow-lined primary in the 40 d orbit. While we cannot fully rule out that variability impacts our results, the simulations using artificial data presented in Appendix C strongly suggest that our tools distinguish well between a static component and an orbital companion with a small K_2. At the very least, our results suggest that the data are not better explained with a

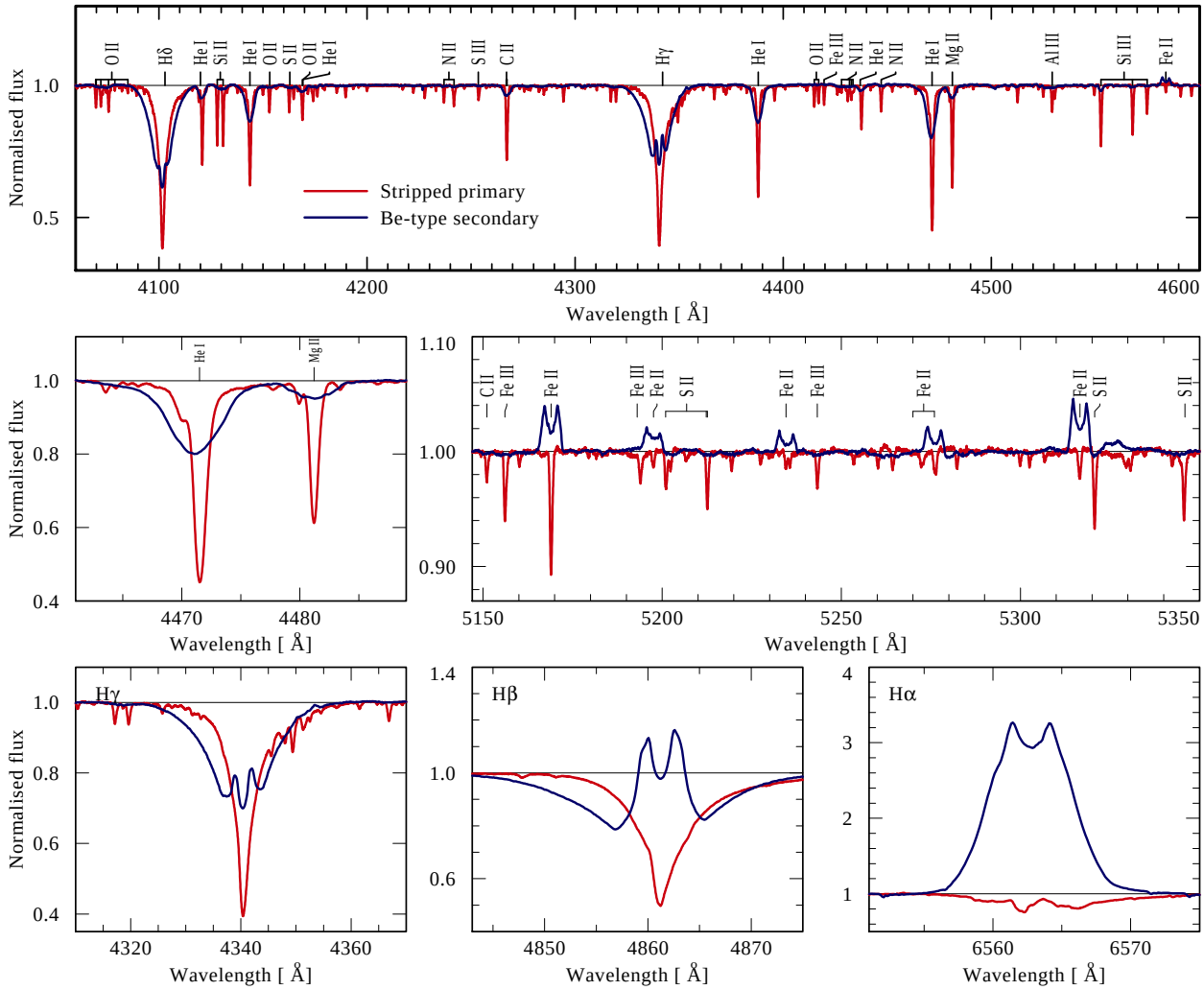

Fig. 7. Disentangled spectra obtained for the narrow-lined primary (red) and the rapidly rotating Be secondary (blue) using the shift-and-add algorithm.

static tertiary Be star, as $\chi^2(K_2 = 0\,\mathrm{km\,s^{-1}})$ is significantly higher than $\chi^2(K_2 = 4\,\mathrm{km\,s^{-1}})$.

The disentangled spectra of the two components using $K_2 = 4\,\mathrm{km\,s^{-1}}$, scaled by the estimated light ratios (see below), are shown in Fig. 7. The disentangled spectra are consistent with the presence of two stellar components: a narrow-lined B-type star (primary) and a rapidly-rotating Be star (secondary), showing characteristic emission in the Balmer lines as well as in Fe II lines. This confirms earlier studies of the system containing a narrow-lined and a broad-lined component (Dachs et al. 1981; Slettebak 1982; Maintz 2003; Rivinius et al. 2020).

We note that virtually all lines observed for the narrow-lined primary exhibit asymmetries, with the right wing of the lines typically being more extended than the left wing. This likely represents the collective effect of pulsational activity throughout the 2004 epoch, as suggested also in Fig. 3 in Sect. 3.4 (see also Aerts et al. 2009). Moreover, the Hα line of the primary, and to a lesser extend the Hβ line, shows indications for emission in its core. The lack of significant absorption in Hα is consistent with the lack of significant variability observed in the core of Hα in the individual observations (see Sect. 3.5). While the observed emission in Hα could be intrinsic to the primary (e.g. due to stellar winds), it could also represent an interaction between the primary and the Be disc (e.g. disc irradiation) that follows the orbit of the primary.

The light ratio cannot be determined from the disentangling process. We therefore estimated it from the two disentangled spectra. We find that both spectra can be reasonably reproduced with models when assuming a light contribution of ≈45% for the primary and ≈55% for the secondary. The light contributions cannot differ from these values by more than ≈20%, because the scaled disentangled spectra would otherwise become unphysical[5]. We thus fixed this light ratio in the further analysis, and note that small changes in the light ratio adopted do not have a strong impact on the determination of the stellar parameters and our final conclusions. The light ratios derived here are similar to the ones reported by Rivinius et al. (2020).

5. Spectral analysis

5.1. The primary narrow-lined B star

5.1.1. Comparison to the B3III giant 18 Peg

Rivinius et al. (2020) reported that the B-type primary is a fairly normal B3III giant and hence adopt stellar parameters derived for the prototypical B3III giant, 18 Peg (Nieva & Przybilla 2014).

[5] For example, assuming a light contribution less than 30% for the primary would cause its Balmer absorption lines in the scaled spectrum to reach negative flux values.

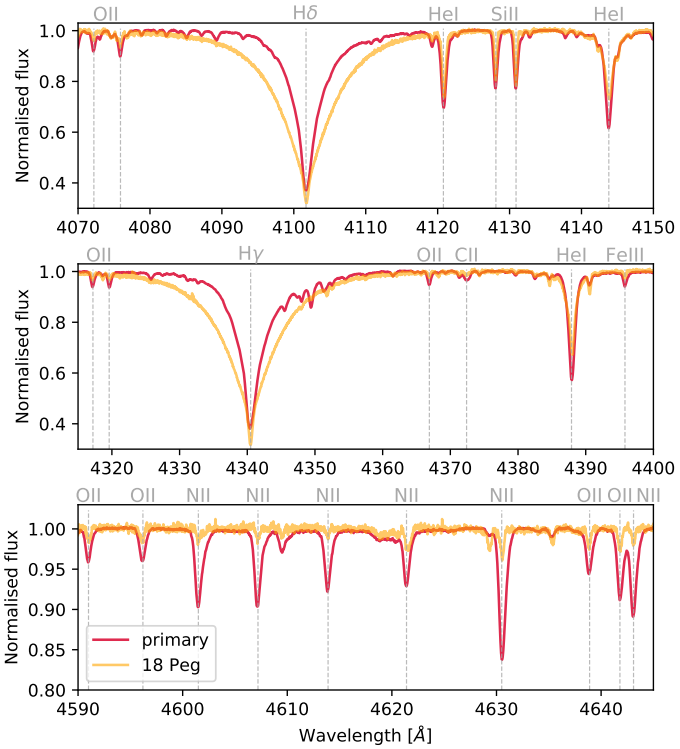

Fig. 8. Comparison of the disentangled primary spectrum scaled for its flux contribution (red) to the spectrum of the prototypical B3 giant 18 Peg (orange). Both spectra are shifted to rest wavelength.

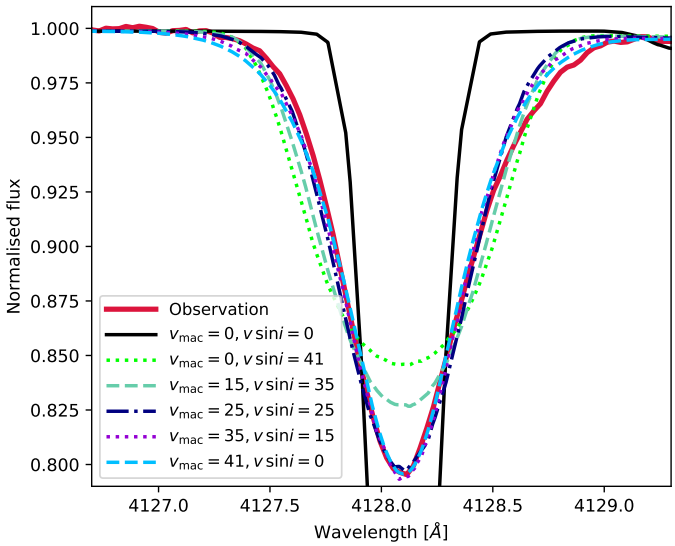

Fig. 9. Comparison between the disentangled spectrum of the Si II λ4128 line with a PoWR model atmosphere for the narrow-lined primary calculated with v_{micro} = 10 km s^{-1} but with different rotation and macroturbulent velocities. The values are given in the legend in km s^{-1}.

We thus qualitatively compare the disentangled and scaled spectrum of the primary to the spectrum of 18 Peg observed with the HERMES spectrograph (Raskin et al. 2011) mounted on the Mercator telescope (wavelength coverage: 3770 to 9000 Å, spectral resolving power: ~85 000) in Fig. 8.

The comparison shows that, while the spectra are in general similar, the Balmer wings of HR 6819 are much narrower than the ones of 18 Peg. This indicates a lower log g in HR 6819. Furthermore it can be seen that O II and especially N II lines are significantly deeper in HR 6819. However, without a detailed spectral analysis, it is not readily clear whether this is due to anomalous surface abundances in the primary of HR 6819 or due to different values of T_{eff} and log g.

5.1.2. Rotation and macroturbulence

The line profiles of the narrow-lined primary are dominated by a "triangular" shape from a radial-tangential broadening profile (Gray 1973; Simón-Díaz & Herrero 2014). This implies that the dominant broadening mechanism is not rotation, but macroturbulent velocity (caused by non-radial pulsations, see Aerts et al. 2009; Bowman et al. 2020; and Sect. 3.4). For slow rotators, and especially in cases where the projected rotational velocity $v \sin i$ and the macroturbulent velocity v_{macro} are comparable, the two parameters are highly degenerate (see e.g. Simón-Díaz & Herrero 2007).

To estimate the broadening parameters we therefore performed a visual comparison between the disentangled spectrum and a model atmosphere calculated with the Potsdam Wolf-Rayet (PoWR) code (see Sect. 5.1.3). Figure 9 illustrates such a comparison for the Si II λ4128 line. It can be seen that, within uncertainties related to both the disentangling procedure and the modelling of the macroturbulence, one cannot distinguish between the fit quality of a non-rotating and a slowly rotating star. Figure 9 also illustrates that $v \sin i$ values larger than approximately 25 km s^{-1} can be excluded. We adopt $v \sin i$ =15 km s^{-1} and v_{macro} = 35 km s^{-1} for the subsequent analysis, but we note that the true $v \sin i$ value may be lower owing to the spectral resolving power.

5.1.3. Stellar parameters and abundances

We compared the disentangled and scaled spectrum of the primary to the BSTAR2006 grid of the model atmosphere code TLUSTY (Hubeny & Lanz 1995; Lanz & Hubeny 2007), which solves the radiative transfer problem in plane-parallel geometry without assuming local thermodynamic equilibrium (non-LTE). The grid covers effective temperatures between 15 and 30 kK in steps of 1 kK and surface gravities between 1.75 and 4.75 in steps of 0.25 dex. The microturbulent velocity is fixed to v_{micro} =2.0 km s^{-1}. We find that the Balmer, helium and most metal lines are well reproduced with models corresponding to $T_{eff} \approx 16-17$ kK and log $g \approx 2.8$ [cgs]. However, several metal lines, especially both Si II and Si III lines, are strongly underestimated by the models. Assuming that the abundance of heavy elements is solar, this indicates that the v_{micro} value is higher than 2 km s^{-1}.

We therefore used an appropriate grid of atmosphere models calculated with the non-LTE Potsdam Wolf-Rayet (PoWR) code (Gräfener et al. 2002; Hamann & Gräfener 2003; Sander et al. 2015). The grid used here is based on an extension of a B-star grid calculated for solar metallicity by Hainich et al. (2019), but with negligible mass-loss rates (log $\dot{M} \lesssim -9.0$ [$M_\odot$ yr^{-1}]). It covers the relevant parameter regime: $15 \leq T_{eff} \leq 19$ kK with a spacing of ΔT_{eff} = 1 kK, $2.4 \leq \log g \leq 3.2$ [cgs] with a spacing of 0.2 dex, and microturbulent velocities of 2, 5 and 10 km s^{-1}.

We find that both v_{micro} = 5 km s^{-1} and v_{micro} = 10 km s^{-1} reproduce the spectra well, with that latter value yielding better results. We therefore fixed v_{micro} = 10 km s^{-1} in the further analysis, noting that the true value may be anywhere between ≈5 and ≈15 km s^{-1}. As possible abundance changes significantly alter the depth of spectral lines, we avoided using temperature

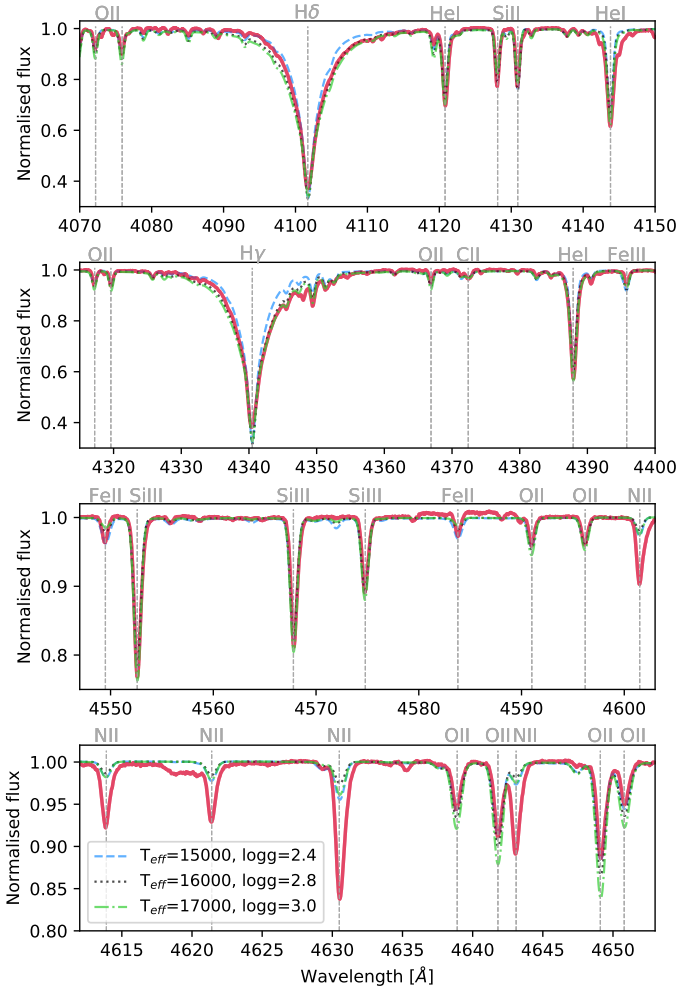

Fig. 10. Comparison between the disentangled primary spectrum scaled for its flux contribution (red) with models for possible $T_{\rm eff} - \log g$ combinations (see legend for the respective $T_{\rm eff}$ and $\log g$ values).

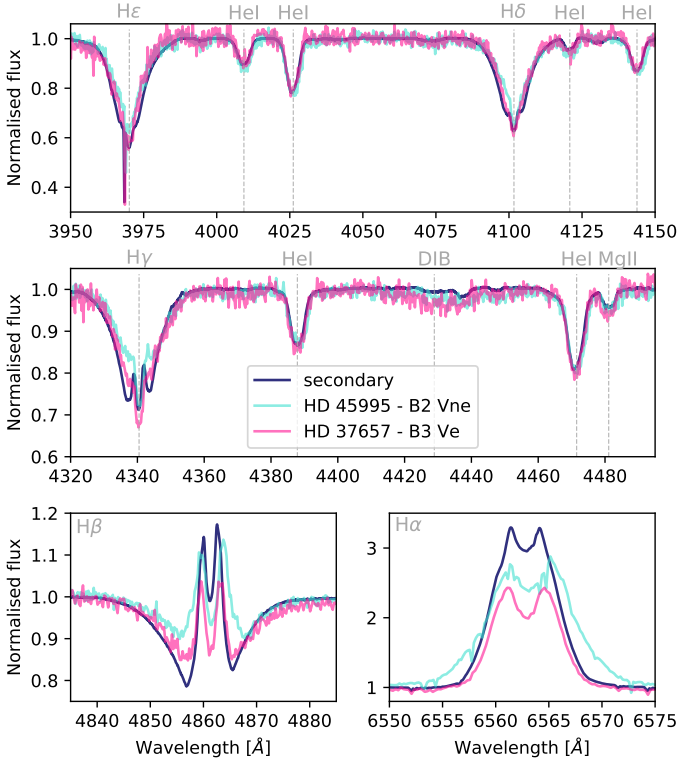

Fig. 11. Comparison between the disentangled spectrum of the secondary (blue) with other representative Be type stars observed with HERMES. The spectra are binned at $\Delta\lambda = 0.2$ Å for clarity.

diagnostics based on two different elements such as the ratio between He I and Mg II lines. Instead, we used the ratio between Si II and Si III as prime temperature diagnostic. As the secondary has Fe II lines in emission (see Fig. 7), which might propagate as additional uncertainty in the line profile of the primary, we refrained from using Fe II to Fe III ratios. By comparing the measured ratios of equivalent widths (EWs) of the observed spectrum to those measured in PoWR models, we find possible $T_{\rm eff} - \log g$ combinations that reproduce the observed Si line ratios within their errors.

Figure 10 shows a comparison between three best-fitting PoWR models with the disentangled spectrum of the primary scaled for its flux contribution. It illustrates that the overall primary spectrum is well reproduced by the model spectra. This is also true for the wings of Balmer and He I lines, which are sensitive to the disentangling procedure and might thus be subject of uncertainty. Given the good overall agreement we argue that this uncertainty is rather small.

The bottom panel of Fig. 10 focuses on several N and O lines. It shows that the N II lines are consistently deeper in the observations than in the models. The opposite effect occurs for the O II lines, which are weaker in the observations. While this is a qualitative comparison and an in-depth abundance analysis is required, it is an indication for an abundance pattern in line with expectations for CNO-processed material. There is, however, no strong indication for an elevated He abundance. We notice the same trend in the abundance pattern of the CNO elements when using TLUSTY.

5.2. The secondary Be component

5.2.1. Comparison to the spectra of classical Be stars

Similarly to the primary, we first qualitatively compare the secondary's spectrum (scaled to the 55% light contribution) to spectra of representative classical Be stars, again observed with HERMES. In Fig. 11 we show the comparison to HD 45995 (B2Vne, Jaschek & Egret 1982) and HD 37657 (B3 Ve, Guetter 1968), for which Zorec et al. (2016) report $v \sin i$ values of $255 \pm 20\,{\rm km\,s^{-1}}$ and $198 \pm 17\,{\rm km\,s^{-1}}$, respectively. In general, the spectrum of the secondary is well reproduced by the Be star spectra. A comparison of the Mg II to the He I line indicates that the secondary is probably of spectral type B2-3 V.

The morphology of the Balmer emission, which primarily depends on the properties of the circumstellar disc and its inclination, is better matched the spectrum of HD 37657 (B3 Ve). The morphology of the Hα line is in agreement with a relatively low inclination ($i \lesssim 45°$, e.g. Rivinius et al. 2013), and is potentially affected by disc truncation induced by the companion (Negueruela & Okazaki 2001; Okazaki et al. 2002).

5.2.2. Rotation and macroturbulence

We determined the projected rotational velocity $v \sin i$ and the macroturbulent velocity $v_{\rm macro}$ of the Be star using the IACOB-BROAD tool (Simón-Díaz & Herrero 2007, 2014). As the He I

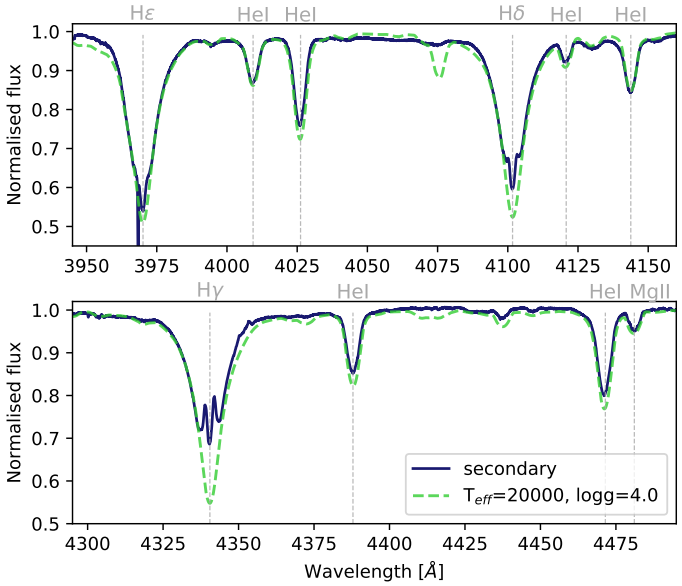

Fig. 12. Comparison between the disentangled spectrum of the secondary (blue) with the best-fit TLUSTY model (green).

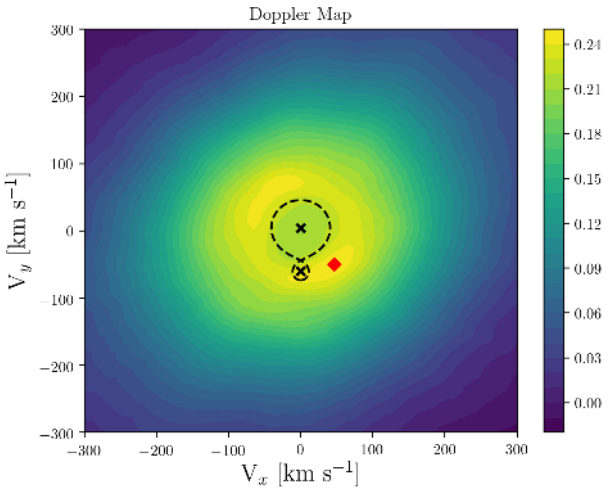

Fig. 13. Doppler map of the Hα line of HR 6819. The crosses correspond to the radial velocity amplitudes of the primary and secondary stars. The shape of the Roche lobe in velocity space (thick dashed line) was calculated for a mass ratio (secondary/primary) of 15.1. The red diamond indicates the maximum of emissivity.

lines are significantly affected by pressure broadening and strong variability, we used the relatively isolated and strong metal lines C II λ4267 and Mg II λ4482. For the C II line, the Fourier method yields $v \sin i = 183\,\mathrm{km\,s^{-1}}$, while the goodness-of-fit yields $v \sin i = 184 \pm 10\,\mathrm{km\,s^{-1}}$ and $v_{\mathrm{macro}} = 70 \pm 30\,\mathrm{km\,s^{-1}}$. For the Mg II line, the Fourier method yields $v \sin i = 166\,\mathrm{km\,s^{-1}}$, while the goodness-of-fit yields $v \sin i = 167 \pm 20\,\mathrm{km\,s^{-1}}$ and $v_{\mathrm{macro}} = 65 \pm 50\,\mathrm{km\,s^{-1}}$. Both lines therefore give comparable results. A weighted average yields $v \sin i = 180 \pm 10\,\mathrm{km\,s^{-1}}$ and $v_{\mathrm{macro}} = 70 \pm 25\,\mathrm{km\,s^{-1}}$. We note that both lines contain a blend of two spectral lines with separations of ≈0.2 Å, such that the derived broadening values may be slightly overestimated.

The high v_{macro} value is consistent with the strong variability observed in the He I lines (Sect. 3.3). Assuming the rotational axis of the Be star is aligned with the orbital inclination of $i = 32°$ (see Sect. 7.1), the $v \sin i$ value derived here implies an equatorial rotation of $v_{\mathrm{eq}} \approx 340\,\mathrm{km\,s^{-1}}$ for the Be component, which amounts to roughly 80% of its estimated critical velocity (Townsend et al. 2004).

5.2.3. Stellar parameters

We compared the disentangled spectrum of the secondary to a grid of TLUSTY models with $v_{\mathrm{micro}} = 2\,\mathrm{km\,s^{-1}}$, which allows us to reproduce the spectrum well. We broadened the spectra according to the $v \sin i$ and v_{macro} described above.

The Balmer and some metal lines such as Fe II are affected by emission and their depth can not be used as diagnostics. We thus resorted to the He I lines and the ratio of the He I λ4472 to the Mg II λ4481 line as a temperature diagnostic. For $\log g$ we focused on the wings of the Balmer and He I lines.

We find that the secondary is best reproduced by a model with $T_{\mathrm{eff}} \simeq 20\,000\,\mathrm{K}$ and a $\log g$ of ~4.0 [cgs] (see Fig. 12). These parameters agree well with the spectral type B2-3 V derived above.

6. Doppler tomography

The spectra of HR 6819 contain an Hα emission line profile reminiscent of that found in Be star spectra. Rivinius et al. (2020) proposed that this emission is attributed to a static Be star that is located further away from the 40 d binary system. Based on our measurement of K_2, we argue here that the Be star is in orbit with the primary on a 40 d period.

To test the consistency of our scenario with the data, we further investigated the origin and distribution of the Hα emissivity by applying the Doppler tomography technique to the Hα line profile. It maps the formation region of these lines in velocity space and requires that the observations fully cover the orbital cycle. We therefore only applied this technique to the 2004 data since the data from 1999 were only collected during half an orbit.

As described in Mahy et al. (2012), the Doppler tomography technique assumes that the radial velocity of any gas flow is stationary in the rotating frame of reference of the system. The velocity of a gas parcel, as seen by the observer, can be expressed by a so-called "S-wave" function,

$$v(\phi) = -v_x \cos(2\pi\phi) + v_y \sin(2\pi\phi) + v_z \quad (1)$$

where ϕ represents the orbital phase, (v_x, v_y) are the velocity coordinates of the gas flow and v_z is the systemic velocity. This relation assumes an x-axis situated between the stars, from the primary to the secondary, and a y-axis pointing in the same direction as the orbital motion of the secondary star (see e.g. Rauw et al. 2002; Linder et al. 2008; Mahy et al. 2012). To reconstruct the images, our method used a Fourier-filtered back-projection algorithm.

The Doppler map (Fig. 13) was computed assuming the radial velocity semi-amplitudes listed in Table 1 ($K_1 = 60.4\,\mathrm{km\,s^{-1}}$, $K_2 = 4.0\,\mathrm{km\,s^{-1}}$ and $\gamma = 9.13\,\mathrm{km\,s^{-1}}$). We have also represented in this map the Roche lobes for the primary (narrow-lined star) and the secondary (Be star). The ring-shaped nature of the emissivity is a signature of an accretion or decretion disc located around the secondary star of the 40 d period system. This is consistent with the secondary being a Be star or a compact object with an accretion disc. In the latter case, a significant X-ray luminosity is expected which was not observed by Berghoefer et al. (1996), and thus excluded by Rivinius et al. (2020).

While the Doppler map indicates the viability of the B+Be model on a 40 d orbit, it does not allow us to test the scenario

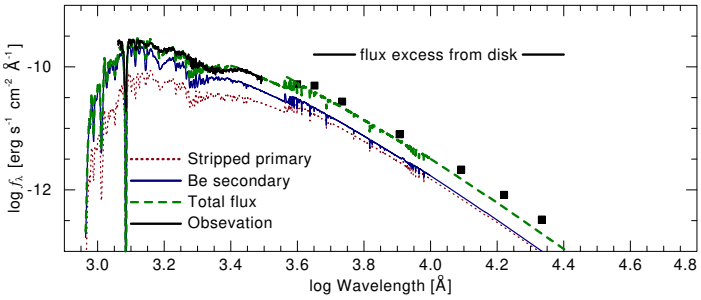

Fig. 14. Comparison between observed photometry and IUE spectra of HR 6819 and the model SED calculated as the sum of two PoWR models with parameters corresponding to those given in Table 1 (see legend).

where the Be star is a distant third companion as the phase coverage provided by the existing data is insufficient to compute a reliable Doppler map in such a scenario.

7. Evolutionary discussion

7.1. Spectroscopic and dynamical masses

The spectroscopic masses can be calculated from $M_{\rm spec} \propto g\,R^2$, where the stellar radius R can be inferred from the Stefan-Boltzmann equation $R \propto L^{1/2}\,T_{\rm eff}^{-2}$, with L the stellar luminosity. With $\log g$ and $T_{\rm eff}$ already inferred for both components, we estimated their luminosities by comparing the observed spectral energy distribution (SED) of HR 6819 with the sum of two PoWR models calculated with the same parameters as those given in Table 1, fixing the light ratio to 45% and 55% in the visual for the narrow-lined primary and Be secondary, respectively (see Sect. 5.1). We used the reddening law given by Cardelli et al. (1989) with a total-to-selective extinction ratio of $R_V = 3.1$. For the distance, we adopted the *Gaia* measurement of $d = 340 \pm 20$ pc provided by Bailer-Jones et al. (2018). The relatively low astrometric excess noise (0.7 mas), the high parallax-over-error value (15), and the re-normalised unit weight error (RUWE) lower than 1.4 (1.14, Lindegren et al. 2018), suggest that, despite being a binary, the measurement of the parallax is not immediately problematic and that the distance estimate is trustworthy. Finally, we adopted UBVI photometric measurements from Ducati (2002) and JHK photometry from Cutri et al. (2003). Moreover, we used two available flux calibrated UV spectra[6] obtained with the International Ultraviolet Explorer (IUE).

The SED comparison is shown in Fig. 14. We find a good agreement for a reddening of $E_{B-V} = 0.1$ mag and luminosities of $\log L/L_\odot = 3.05$ and 3.35 for the primary and secondary, respectively. Significant flux excess is observed in the infrared and to a lesser extent in the visual, which most likely stems from the disc of the Be component (e.g. Cochetti et al. 2019).

Using the derived luminosities, we estimated the spectroscopic masses. Interestingly, the spectroscopic mass of the narrow-lined component turns out to be $M_{\rm spec,1} = 0.4^{+0.3}_{-0.1}\,M_\odot$. This value is clearly not in agreement with the primary being a standard B-type main sequence (MS) star, as assumed by Rivinius et al. (2020). Instead, the mass, together with the enhanced N-abundance, suggests that the narrow-lined B-type component is another example of a thermally-unstable stripped star, similarly to LB-1 (Irrgang et al. 2020; Shenar et al. 2020). Moreover, combining this mass estimate with the binary mass function $f_{\rm M} = 0.96\,M_\odot$ implies that the minimum mass of the companion on the 40 d orbit is $\approx$1.5 $M_\odot$. Hence, even if the secondary is not the Be star, as proposed here, but rather an unseen companion, one cannot immediately rule out the possibility that it is a faint MS star or a neutron star, instead of a BH.

The luminosity of the Be star is broadly consistent with its estimated spectral type of B2-3 V (Hohle et al. 2010). The spectroscopic mass of the secondary is found to be around 15 times larger than the one of the primary, that is $M_{\rm spec,2} = 6^{+5}_{-3}\,M_\odot$, where the conservative $\log g$ error is used. This mass is also in agreement with typical values reported for Be stars of comparable spectral classes (Hohle et al. 2010).

By calibrating the mass of the secondary Be star to a mass typical for its spectral type, $M_2 = 7 \pm 2\,M_\odot$ (Hohle et al. 2010), we can obtain a measurement of the orbital inclination and the dynamical mass of the narrow-lined star, which is independent of the spectroscopic mass estimated above. This yields an inclination of $i = 32 \pm 4°$ and $M_{\rm 1,dyn} = 0.46 \pm 0.24\,M_\odot$, in excellent agreement with our spectroscopic mass estimate. In summary, the present analysis supports a formation scenario for HR 6819 similar to that proposed for LB-1 by Shenar et al. (2020), involving a past binary mass-exchange event that led to the formation of the stripped star and its rapidly-rotating Be companion.

7.2. Evolutionary history

If the system is indeed composed of a bloated stripped star that recently donated mass to the Be star, its current orbital properties can be used to assess the initial conditions of the progenitor system. Assuming circular orbits, a constant mass transfer efficiency, and ignoring other mechanisms for angular momentum loss from the system, the orbital period can be computed analytically as a function of the mass ratio (Soberman et al. 1997). For the case of conservative mass transfer one has that

$$\frac{P}{P_r} = \left(\frac{q}{q_r}\right)^{-3} \left(\frac{1+q}{1+q_r}\right)^{6}, \tag{2}$$

where P_r and $q_r \equiv M_{\rm Be}/M_{\rm stripped}$ represent the orbital period and mass ratio at a particular reference point, which we take to be the currently observed values. In the case where mass transfer is fully non-conservative, with the ejected mass carrying away the specific angular momentum of the accreting star, the evolution of the orbital period is given by[7]

$$\frac{P}{P_r} = \left(\frac{q}{q_r}\right)^{5} \left(\frac{1+q}{1+q_r}\right)^{-2} e^{3(q_r-q)/q_r q}. \tag{3}$$

Both of these expressions allow us to determine the orbital period of the system at a previous point in time, when its mass ratio was smaller.

Figure 15 shows the result of evaluating Eqs. (2) and (3) for different values of the currently observed mass ratio within our range of uncertainty. Although we do not know the mass ratio at birth, the stripped star had to be the most massive component ($q < 1$ with our definition of mass ratio). If we assume the initial mass ratio was $q = 1/3$, then the initial orbital period needs to be $\lesssim$2 d to explain its current value. Moreover, fully non-conservative mass transfer requires initial orbital periods smaller

[6] IDs: SWP31220, SWP31220, PI: T. Snow.

[7] The definition of q in Eq. (3) is the inverse of the one used in Soberman et al. (1997). It also corrects a typo in Eq. (22) of that work.

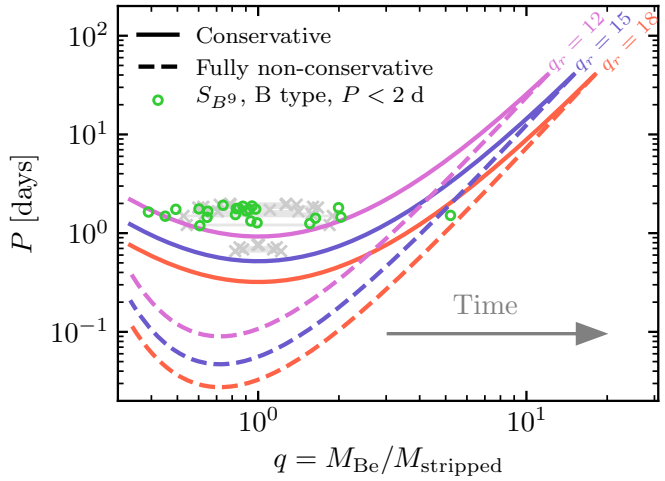

Fig. 15. Past orbital evolution of the system assuming present-day mass ratios of q = 12, 15 and 18. During mass transfer phases time increases towards the right in this figure. For each curve the right-most point represents the currently observed values, while the left-most point corresponds to an arbitrary choice of $q = 1/3$. Circles are a selection of detached and semidetached systems from the S_{B^9} catalogue. Crosses are systems from the same catalogue for which it is unclear if the binary has undergone a mass ratio inversion, so two points are included per system with inverse values for q (see text for details).

than 10 h. For either case, the short initial periods required are indicative of the system having undergone Roche-lobe overflow during the main sequence (Case A mass transfer). This can help explain the extreme mass ratio of the system, as Case A evolution leads to smaller masses for the resulting stripped stars compared to binaries that interact after the main sequence (Wellstein et al. 2001).

To check for the existence of known binary systems that can be potential progenitors for HR 6819, we consider all double-lined binaries contained in the S_{B^9} catalogue of spectroscopic binaries (Pourbaix et al. 2004) with a period of less than 2 d. In addition, to exclude systems with either too high or too low total masses, we only take into account binaries with one B-type component, and without an O-type component. Although this gives us enough information to determine the mass ratios, we do not know if the system has interacted and potentially undergone a mass ratio inversion. To remove this uncertainty we consider detached binaries that would correspond to a pre-interaction system with $q < 1$, and semi-detached binaries with a Roche-lobe filling secondary that correspond to the phase after mass inversion with $q > 1$. For all other binaries that do not fall into either of these categories we cannot assess if there has been a mass ratio inversion, so we consider both possibilities for the mass ratio (see Appendix D for a full list of the systems). As shown in Fig. 15, there are various observed systems that, through conservative mass transfer, can lead to a binary with a mass ratio comparable to the one we derive for HR 6819. Notably, there are no detached systems that could serve as progenitors through non-conservative mass transfer.

Using Eqs. (2) or (3) as a guide we can choose initial properties of the system to attempt to model it using a stellar evolution code. As a simple example, we consider here a binary system with initial masses of 6 $M_\odot$ and 2 $M_\odot$ at a period of 2 d undergoing fully conservative mass transfer. The model is computed using the `MESA` code for stellar evolution (Paxton et al. 2011, 2013, 2015, 2018, 2019). Full details of our simulation settings and physics assumptions, as well as necessary steps to reproduce this simulation, are provided in Appendix E. The evolution of the donor star in this system is illustrated in Fig. 16. The star evolves unperturbed until it fills its Roche-lobe after 55 Myr of evolution. At this point the star is still on the main sequence, resulting in a phase of Case A mass transfer that lasts until the donor depletes its central hydrogen. This phase lasts 23 Myr and reduces the mass of the donor to 1.5 $M_\odot$. After core-hydrogen depletion, another phase of mass transfer ensues (commonly referred to as Case AB mass transfer) that lasts for 6.7 Myr and reduces its mass to 0.59 $M_\odot$. The star then detaches and evolves towards increasing T_eff, reaching its maximum value after 1 Myr. For the last 12 Myr of the simulation the stripped star burns helium at its core, but before it depletes it, the accreting star, which now has a mass of 7.4 $M_\odot$, finishes its main sequence evolution. The further evolution of the model is not computed, but a phase of inverse mass transfer is expected which, owing to the extreme mass ratio, would be unstable.

In this simulation, the evolutionary stage that corresponds to the B star in HR 6819 is right after detachment from Case AB mass transfer. When the stripped star in the model reaches $T_\mathrm{eff} = 16$ kK, it has $\log L/L_\odot = 2.99$ and $\log g = 2.97$ [cgs], while the companion has $T_\mathrm{eff} = 22$ kK, $\log L/L_\odot = 3.57$ and $\log g = 4.34$ [cgs]. The mass ratio at this stage is $q = 12.5$ and the orbital period is of 38.9 days. All these values are comparable to the currently observed ones, despite not having done an extensive parameter search to find a progenitor system. One important aspect that appears to be inconsistent with the observations though, is that the mass fraction of helium at the surface of the stripped star is predicted to be $Y = 0.87$, whereas no helium enhancement is observed in spectroscopy. It is unclear which physical processes could explain this discrepancy. Gravitational settling can lower the abundance of elements heavier than hydrogen at the surface (Iben & MacDonald 1985), but including this effect in our simulation shows that it does not operate on the brief 1 Myr phase of contraction. A more speculative scenario is that mass being lost by the Be star through a decretion disc contaminates the surface of the stripped star with material that is hydrogen-rich.

Given the similarities of our model to the observed system, one can use it to roughly estimate the rarity of observing such systems with a bloated stripped star right after mass transfer. By simply taking ratios of the lifetimes of the different phases, compared to the 1 Myr period after mass transfer when the star evolves to higher T_eff, one finds that for each system such as HR 6819, among the progenitor systems one expects 55 pre-interaction binaries, 23 systems undergoing mass transfer on the MS, about 7 systems undergoing case AB mass transfer, and 11 systems composed of a compact core-helium burning star and a rapidly rotating B star. The latter are potentially observable as a single Be star given the low mass and low luminosity of the core-helium burning companion. The post-mass transfer phase that corresponds to HR 6819 represents about 1% of the total lifetime, so for every system similar to HR 6819 one would expect about 100 systems in one of the other evolutionary stages. While rare, this is by no means an exceptional occurrence rate. In the future, we expect the HR 6819 system to merge when the Be star depletes the hydrogen in its core, owing to the extreme mass ratio of the system.

8. Conclusions

We performed a detailed spectroscopic and evolutionary analysis of HR 6819, which was recently proposed by Rivinius et al. (2020) to be a hierarchical triple system comprising a

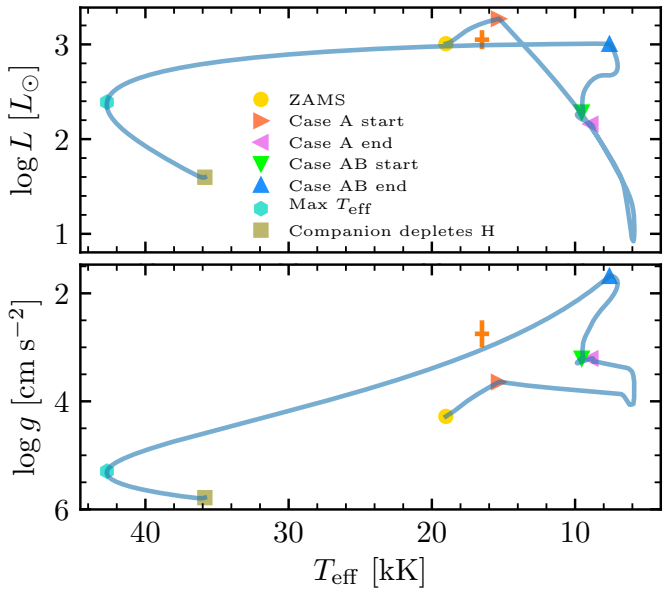

Fig. 16. Evolution in the Hertzsprung-Russel (*top panel*) and Kiel diagrams (*bottom panel*) of the donor star of a binary system with initial masses of 6 $M_\odot$ and 2 $M_\odot$ and orbital period of 2 days. The orange error bars indicate the observed values of the B star in HR 6819, and different symbols indicate different evolutionary stages (see legend).

BH+B-giant binary on a 40 d orbit and a distant Be tertiary. Based on the available spectroscopic observations of HR 6819, our spectral disentangling implies that the spectral features of the Be star (Balmer lines, photospheric He I lines, and disc Fe II and O II lines) move in anti-phase with the narrow spectral features of the B-type primary. We derived RV amplitudes of $K_1 = 60.4 \pm 1.0\,\mathrm{km\,s^{-1}}$ and $K_2 = 4.0 \pm 0.8\,\mathrm{km\,s^{-1}}$, which translate to an extreme mass ratio between the two components of $M_2/M_1 \approx 15 \pm 3$. We thus conclude that the Be star is not a tertiary, but instead the secondary in the 40 d period system. Our spectroscopic analysis shows that the primary has $T_{\rm eff} \approx 16 \pm 1$ kK and $\log g \approx 2.8 \pm 0.2$ [cgs]. We find a high macro-turbulent velocity of $v_{\rm macro} = 35 \pm 5\,\mathrm{km\,s^{-1}}$ and can only report an upper limit on the rotational velocity $v \sin i \lesssim 25\,\mathrm{km\,s^{-1}}$. The secondary spectrum resembles the typical spectrum of a Be star and the comparison to classical Be stars indicates that it is of spectral type B2-3 Ve. This agrees with the estimated atmospheric parameters of $T_{\rm eff} \approx 20 \pm 2$ kK and $\log g \approx 4.0 \pm 0.3$ [cgs]. We derive $v \sin i = 185 \pm 20\,\mathrm{km\,s^{-1}}$ and $v_{\rm macro} = 70 \pm 25\,\mathrm{km\,s^{-1}}$. The comparably high values of $v_{\rm macro}$ in both stars are in line with the observation of strong variability in both components on different timescales, with observed short- and medium-term variability consistent with non-radial pulsations (Aerts et al. 2009; Rivinius et al. 2020).

Based on luminosities derived from a SED fit, we estimated the spectroscopic masses of the two stars. We find that the spectroscopic mass of the primary is $M_{\rm spec,1} = 0.4^{+0.3}_{-0.1}\,M_\odot$ while the spectroscopic mass of the secondary is $M_{\rm spec,2} = 6^{+5}_{-3}\,M_\odot$. Our analysis suggests that HR 6819 is a binary system containing a stripped star and a Be star, bearing similarity to the recently discovered binary LB-1 (Liu et al. 2019; Irrgang et al. 2020; Shenar et al. 2020). By modelling the system with MESA, we show that we can reproduce the currently observed parameters with a tight progenitor system that has undergone Case A mass transfer. One important caveat of our model is that we find no indications for the strong enrichment in helium which is predicted by the models. We do, however, observe indications for an enhanced nitrogen abundance which agrees with the predictions.

This work shows that the HR 6819 system can be explained without invoking the presence of a stellar-mass BH. Considering the low value of K_2 derived here and the time coverage of the data, we cannot fully exclude that the Be star is stationary (Appendix C), nor can we fully exclude the presence of additional components on an even shorter orbit (Sect. 3.3). Contemporaneously with this work, two additional, independent studies were completed that challenge the interpretation of HR 6819 as a triple system containing a BH. While Safarzadeh et al. (2020) argue that a triple configuration is very unlikely based on statistical, dynamical, and evolutionary arguments, El-Badry & Quataert (2020b) perform a similar spectroscopic analysis and reach the same conclusions as presented in this work.

A final test to reveal the configuration of the system and the nature of its components can only be given by an independent measurement of the separation between the visible components. Given the small distance to the system, a combination of interferometric and high-contrast imaging observations could help to test all different scenarios. This opens an unprecedented observing window in the important parameter space to constrain the nature of this intriguing system.

Acknowledgements. Based on observations obtained with the HERMES spectrograph, which is supported by the Research Foundation – Flanders (FWO), Belgium, the Research Council of KU Leuven, Belgium, the Fonds National de la Recherche Scientifique (F.R.S.-FNRS), Belgium, the Royal Observatory of Belgium, the Observatoire de Genève, Switzerland and the Thüringer Landessternwarte Tautenburg, Germany. This work has made use of the BeSS database, operated at LESIA, Observatoire de Meudon, France: http://basebe.obspm.fr. We thank T. Bohlsen and P. Luckas for uploading their spectra to the BeSS database. The research leading to these results has received funding from the European Research Council (ERC) under the European Union's Horizon 2020 research and innovation programme (grant agreement numbers 772225: MULTIPLES and 670519: MAMSIE), the FWO Odysseus program under project G0F8H6N and the FWO junior fellowship 12ZY520N. PM would like to thank Alina Istrate for helpful discussion.

References

Abbott, B. P., Abbott, R., Abbott, T. D., et al. 2019, Phys. Rev. X, 9, 031040
Abdul-Masih, M., Sana, H., Sundqvist, J., et al. 2019, ApJ, 880, 115
Abdul-Masih, M., Banyard, G., Bodensteiner, J., et al. 2020, Nature, 580, E11
Aerts, C., Puls, J., Godart, M., & Dupret, M. A. 2009, A&A, 508, 409
Aerts, C., Christensen-Dalsgaard, J., & Kurtz, D. W. 2010, Asteroseismology (Germany: Springer Science+Business Media B.V.)
Andersen, J. 1983, A&A, 118, 255
Andersen, J., Clausen, J. V., Gimenez, A., & Nordstroem, B. 1983, A&A, 128, 17
Andersen, J., Clausen, J. V., Nordstrom, B., & Popper, D. M. 1985, A&A, 151, 329
Angulo, C., Arnould, M., Rayet, M., et al. 1999, Nucl. Phys. A, 656, 3
Aoki, W., Tominaga, N., Beers, T. C., Honda, S., & Lee, Y. S. 2014, Science, 345, 912
Baade, D. 1984, A&A, 135, 101
Bailer-Jones, C. A. L., Rybizki, J., Fouesneau, M., Mantelet, G., & Andrae, R. 2018, AJ, 156, 58
Bakiş, V., Bulut, Á., Bilir, S., et al. 2010, PASJ, 62, 1291
Bakis, H., Bakis, V., Bilir, S., et al. 2011, PASJ, 63, 1079
Balona, L. A., Aerts, C., & Štefl, S. 1999, MNRAS, 305, 519
Belczynski, K., Kalogera, V., & Bulik, T. 2002, ApJ, 572, 407
Bell, S. A., & Malcolm, G. J. 1987, MNRAS, 226, 899
Bell, S. A., Kilkenny, D., & Malcolm, G. J. 1987, MNRAS, 226, 879
Berghoefer, T. W., Schmitt, J. H. M. M., & Cassinelli, J. P. 1996, A&AS, 118, 481
Bjorkman, K. S., Miroshnichenko, A. S., McDavid, D., & Pogrosheva, T. M. 2002, ApJ, 573, 812
Bowman, D. M., Burssens, S., Pedersen, M. G., et al. 2019, Nat. Astron., 3, 760

Bowman, D. M., Burssens, S., Simón-Díaz, S., et al. 2020, A&A, 640, A36
Bromm, V., Yoshida, N., Hernquist, L., & McKee, C. F. 2009, Nature, 459, 49
Buscombe, W., & Morris, P. M. 1960, MNRAS, 121, 263
Cardelli, J. A., Clayton, G. C., & Mathis, J. S. 1989, ApJ, 345, 245
Casares, J., Negueruela, I., Ribó, M., et al. 2014, Nature, 505, 378
Clausen, J. V., Helt, B. E., Giménez, A., et al. 2007, A&A, 461, 1065
Cochetti, Y. R., Arcos, C., Kanaan, S., et al. 2019, A&A, 621, A123
Cutri, R. M., Skrutskie, M. F., van Dyk, S., et al. 2003, VizieR Online Data Catalog: II/246
Cyburt, R. H., Amthor, A. M., Ferguson, R., et al. 2010, ApJS, 189, 240
Dachs, J., Eichendorf, W., Schleicher, H., et al. 1981, A&AS, 43, 427
Dachs, J., Hanuschik, R., Kaiser, D., et al. 1986, A&AS, 63, 87
Değirmenci, Ö. L., Gülmen, Ö., Sezer, C., Güdür, N., & Erdem, A. 1996, Ap&SS, 241, 327
de Mink, S. E., Langer, N., Izzard, R. G., Sana, H., & de Koter, A. 2013, ApJ, 764, 166
Dervisoglu, A., Çakirli, Ö., Ibanoglu, C., & Sipahi, E. 2011, Rev. Mex. Astron. Astrofis., 47, 297
Di Carlo, U. N., Giacobbo, N., Mapelli, M., et al. 2019, MNRAS, 487, 2947
Doazan, V., Marlborough, J. M., Morossi, C., et al. 1986, A&A, 158, 1
Draper, Z. H., Wisniewski, J. P., Bjorkman, K. S., et al. 2011, ApJ, 728, L40
Drechsel, H., Rahe, J., Wargau, W., & Wolf, B. 1982, A&A, 110, 246
Ducati, J. R. 2002, VizieR Online Data Catalog: II/237
Dunstall, P. R., Dufton, P. L., Sana, H., et al. 2015, A&A, 580, A93
El-Badry, K., & Quataert, E. 2020a, MNRAS, 493, L22
El-Badry, K., & Quataert, E. 2020b, MNRAS, submitted [arXiv:2006.11974]
Fragione, G., Grishin, E., Leigh, N. W. C., Perets, H. B., & Perna, R. 2019, MNRAS, 488, 47
Giuricin, G., & Mardirossian, F. 1981, A&A, 94, 201
Giuricin, G., Mardirossian, F., & Mezzetti, M. 1980, A&AS, 39, 255
González, J. F., & Levato, H. 2006, A&A, 448, 283
Gräfener, G., Koesterke, L., & Hamann, W. R. 2002, A&A, 387, 244
Gray, D. F. 1973, ApJ, 184, 461
Grevesse, N., Noels, A., & Sauval, A. J. 1996, in Cosmic Abundances, eds. S. S. Holt, & G. Sonneborn, ASP Conf. Ser., 99, 117
Guetter, H. H. 1968, PASP, 80, 197
Hadrava, P. 1995, A&AS, 114, 393
Hainich, R., Ramachandran, V., Shenar, T., et al. 2019, A&A, 621, A85
Hamann, W. R., & Gräfener, G. 2003, A&A, 410, 993
Harries, T. J., Hilditch, R. W., & Hill, G. 1998, MNRAS, 295, 386
Hiltner, W. A., Garrison, R. F., & Schild, R. E. 1969, ApJ, 157, 313
Hohle, M. M., Neuhäuser, R., & Schutz, B. F. 2010, Astron. Nachr., 331, 349
Holmgren, D. E., Hill, G., & Fisher, W. 1990, A&A, 236, 409
Hubeny, I., & Lanz, T. 1995, ApJ, 439, 875
Iben, I., Jr., & MacDonald, J. 1985, ApJ, 296, 540
Iglesias, C. A., & Rogers, F. J. 1996, ApJ, 464, 943
Ilijić, S. 2017, Astrophysics Source Code Library [record ascl:1705.012]
Ilijić, S., Hensberge, H., Pavlovski, K., & Freyhammer, L. M. 2004, ASP Conf. Ser., 318, 111
Irrgang, A., Geier, S., Kreuzer, S., Pelisoli, I., & Heber, U. 2020, A&A, 633, L5
Jamet, L., Pérez, E., Cerviño, M., et al. 2004, A&A, 426, 399
Jaschek, M., & Egret, D. 1982, in Be Stars, eds. M. Jaschek, & H. G. Groth, IAU Symp., 98, 261
Jeffreys, K. W. 1980, A&AS, 42, 285
Johnston, C., Pavlovski, K., & Tkachenko, A. 2019, A&A, 628, A25
Kaufer, A., Stahl, O., Tubbesing, S., et al. 1999, The Messenger, 95, 8
Khaliullin, K. F., & Khaliullina, A. I. 2006, Astron. Rep., 50, 358
Khokhlov, S. A., Miroshnichenko, A. S., Zharikov, S. V., et al. 2018, ApJ, 856, 158
Kippenhahn, R., Ruschenplatt, G., & Thomas, H. C. 1980, A&A, 91, 175
Kobulnicky, H. A., Kiminki, D. C., Lundquist, M. J., et al. 2014, ApJS, 213, 34
Kolb, U., & Ritter, H. 1990, A&A, 236, 385
Koubský, P., Kotková, L., Votruba, V., Šlechta, M., & Dvořáková, Š. 2012, A&A, 545, A121
Lacy, C. H. 1977, ApJ, 212, 132
Lacy, C. H. S. 1997, AJ, 113, 1091
Lacy, C. H., & Frueh, M. L. 1985, ApJ, 295, 569
Langer, N. 2012, ARA&A, 50, 107
Langer, N., Fricke, K. J., & Sugimoto, D. 1983, A&A, 126, 207
Langer, N., Schürmann, C., Stoll, K., et al. 2020, A&A, 638, A39
Lanz, T., & Hubeny, I. 2007, ApJS, 169, 83
Lefèvre, L., Marchenko, S. V., Moffat, A. F. J., & Acker, A. 2009, A&A, 507, 1141
Lindegren, L., Hernández, J., Bombrun, A., et al. 2018, A&A, 616, A2
Linder, N., Rauw, G., Martins, F., et al. 2008, A&A, 489, 713
Liu, Q. Z., van Paradijs, J., & van den Heuvel, E. P. J. 2006, A&A, 455, 1165
Liu, J., Zhang, H., Howard, A. W., et al. 2019, Nature, 575, 618
Liu, J., Zheng, Z., Soria, R., et al. 2020, ApJ, submitted [arXiv:2005.12595]
Lorenz, R., Mayer, P., & Drechsel, H. 1999, A&A, 345, 531
Mahy, L., Gosset, E., Sana, H., et al. 2012, A&A, 540, A97
Maintz, M. 2003, PhD Thesis, Univ. of Heidelberg, Germany
Mandel, I., & de Mink, S. E. 2016, MNRAS, 458, 2634
Marchant, P., Langer, N., Podsiadlowski, P., Tauris, T. M., & Moriya, T. J. 2016, A&A, 588, A50
Marchenko, S. V., Moffat, A. F. J., & Eenens, P. R. J. 1998, PASP, 110, 1416
Moe, M., & Di Stefano, R. 2017, ApJS, 230, 15
Negueruela, I., & Okazaki, A. T. 2001, A&A, 369, 108
Neiner, C., de Batz, B., Cochard, F., et al. 2011, AJ, 142, 149
Nieva, M.-F., & Przybilla, N. 2014, A&A, 566, A7
Nishikawa, H., Kovetz, E. D., Kamionkowski, M., & Silk, J. 2019, Phys. Rev. D, 99, 043533
Okazaki, A. T. 1991, PASJ, 43, 75
Okazaki, A. T., Bate, M. R., Ogilvie, G. I., & Pringle, J. E. 2002, MNRAS, 337, 967
Öztürk, O., Soydugan, F., & Çiçek, C. 2014, New Astron., 30, 100
Paczyński, B. 1967, Acta Atron., 17, 355
Pápics, P. I., Tkachenko, A., Van Reeth, T., et al. 2017, A&A, 598, A74
Paxton, B., Bildsten, L., Dotter, A., et al. 2011, ApJS, 192, 3
Paxton, B., Cantiello, M., Arras, P., et al. 2013, ApJS, 208, 4
Paxton, B., Marchant, P., Schwab, J., et al. 2015, ApJS, 220, 15
Paxton, B., Schwab, J., Bauer, E. B., et al. 2018, ApJS, 234, 34
Paxton, B., Smolec, R., Schwab, J., et al. 2019, ApJS, 243, 10
Podsiadlowski, P., Joss, P. C., & Hsu, J. J. L. 1992, ApJ, 391, 246
Pols, O., Cote, J., Waters, L. B. F. M., & Heise, J. 1991, A&A, 241, 419
Popper, D. M. 1987, AJ, 93, 672
Pourbaix, D., Tokovinin, A. A., Batten, A. H., et al. 2004, A&A, 424, 727
Qian, S. B., Liao, W. P., & Fernández Lajús, E. 2008, ApJ, 687, 466
Raskin, G., Van Winckel, H., Hensberge, H., et al. 2011, A&A, 526, A69
Rauw, G., Crowther, P. A., Eenens, P. R. J., Manfroid, J., & Vreux, J. M. 2002, A&A, 392, 563
Rivinius, T., Baade, D., & Štefl, S. 2003, A&A, 411, 229
Rivinius, T., Carciofi, A. C., & Martayan, C. 2013, A&ARv, 21, 69
Rivinius, T., Baade, D., Hadrava, P., Heida, M., & Klement, R. 2020, A&A, 637, L3
Rogers, F. J., & Nayfonov, A. 2002, ApJ, 576, 1064
Russo, G., Milano, L., & Maceroni, C. 1982, A&A, 109, 368
Safarzadeh, M., Toonen, S., & Loeb, A. 2020, ApJ, 897, L29
Sana, H., de Mink, S. E., de Koter, A., et al. 2012, Science, 337, 444
Sana, H., de Koter, A., de Mink, S. E., et al. 2013, A&A, 550, A107
Sander, A., Shenar, T., Hainich, R., et al. 2015, A&A, 577, A13
Shao, Y., & Li, X.-D. 2019, ApJ, 885, 151
Shenar, T., Hainich, R., Todt, H., et al. 2018, A&A, 616, A103
Shenar, T., Bodensteiner, J., Abdul-Masih, M., et al. 2020, A&A, 639, L6
Simón-Díaz, S., & Herrero, A. 2007, A&A, 468, 1063
Simón-Díaz, S., & Herrero, A. 2014, A&A, 562, A135
Simón-Díaz, S., Godart, M., Castro, N., et al. 2017, A&A, 597, A22
Simón-Díaz, S., Maíz Apellániz, J., Lennon, D. J., et al. 2020, A&A, 634, L7
Slettebak, A. 1982, ApJS, 50, 55
Soberman, G. E., Phinney, E. S., & van den Heuvel, E. P. J. 1997, A&A, 327, 620
Štefl, S., Rivinius, T., Carciofi, A. C., et al. 2009, A&A, 504, 929
Švaříček, P., Wolf, M., Claret, A., et al. 2008, A&A, 477, 615
Terrell, D., Munari, U., & Siviero, A. 2007, MNRAS, 374, 530
Thompson, T. A., Kochanek, C. S., Stanek, K. Z., et al. 2019, Science, 366, 637
Townsend, R. H. D., Owocki, S. P., & Howarth, I. D. 2004, MNRAS, 350, 189
Ulaş, B., Kalomeni, B., Keskin, V., Köse, O., & Yakut, K. 2012, New Astron., 17, 296
van Antwerpen, C., & Moon, T. 2010, MNRAS, 401, 2059
Vanbeveren, D., & De Loore, C. 1994, A&A, 290, 129
van den Heuvel, E. P. J., & Tauris, T. M. 2020, Science, 368, eaba3282
Wang, L., Gies, D. R., & Peters, G. J. 2018, ApJ, 853, 156
Wellstein, S., Langer, N., & Braun, H. 2001, A&A, 369, 939
Wisniewski, J. P., Draper, Z. H., Bjorkman, K. S., et al. 2010, ApJ, 709, 1306
Yi, T., Sun, M., & Gu, W.-M. 2019, ApJ, 886, 97
Zhao, E., Qian, S., Li, L., et al. 2018, PASP, 130, 084205
Zorec, J., Frémat, Y., Domiciano de Souza, A., et al. 2016, A&A, 595, A132

Appendix A: Journal of the observations

Table A.1 provides a journal of observations including exposure times, signal-to-noise (S/N) ratios and RVs of the narrow-lined primary. In Table A.2 we give an overview over the additional BeSS spectra used together with their exposure times and resolving powers.

Table A.1. Journal of the observations of HR 6819.

HJD [d]	Time [s]	*S/N*	RV_1 [km s^{-1}]
2451373.676	300	150	-39.0 ± 4.5
2451374.675	300	290	-43.6 ± 4.5
2451375.653	300	300	-41.6 ± 4.5
2451376.724	1800	200	-30.9 ± 4.5
2451378.682	1500	280	-27.7 ± 4.4
2451380.824	360	240	-14.8 ± 4.4
2451383.673	300	270	12.1 ± 4.4
2451384.743	300	230	24.1 ± 4.4
2451385.759	300	200	32.8 ± 4.5
2451390.745	300	300	62.9 ± 4.9
2451393.627	300	200	68.9 ± 5.1
2451394.758	300	220	65.5 ± 5.0
2453138.847	150	320	-7.7 ± 4.4
2453139.682	150	300	-14.5 ± 4.4
2453143.808	150	230	-50.0 ± 4.6
2453144.753	150	340	-54.4 ± 4.6
2453149.762	150	320	-51.1 ± 4.6
2453149.765	150	320	-51.1 ± 4.6
2453154.669	150	300	-21.5 ± 4.4
2453159.804	150	340	18.5 ± 4.4
2453160.686	150	370	28.5 ± 4.5
2453162.862	150	230	42.0 ± 4.5
2453185.551	150	400	-52.6 ± 4.6
2453187.666	150	330	-51.6 ± 4.6
2453188.687	150	360	-53.7 ± 4.6
2453190.704	150	310	-49.3 ± 4.6
2453194.691	150	350	-25.6 ± 4.4
2453195.563	150	350	-14.7 ± 4.4
2453196.550	150	270	-2.7 ± 4.4
2453197.670	150	330	8.1 ± 4.4
2453199.570	150	310	26.8 ± 4.5
2453202.645	150	330	51.4 ± 4.7
2453204.513	150	340	66.3 ± 5.0
2453205.697	150	320	69.8 ± 5.2
2453207.501	150	250	74.9 ± 5.3
2453226.596	150	290	-52.0 ± 4.6
2453230.490	150	420	-45.9 ± 4.5
2453231.569	150	360	-40.5 ± 4.5
2453232.502	150	300	-39.7 ± 4.5
2453239.494	150	420	21.2 ± 4.4
2453240.602	150	300	29.6 ± 4.5
2453243.515	150	400	56.9 ± 4.8
2453244.551	150	370	62.4 ± 4.9
2453245.510	150	430	67.0 ± 5.1
2453246.619	150	310	64.7 ± 5.0
2453247.553	150	320	64.4 ± 5.0
2453248.522	150	430	69.4 ± 5.1
2453254.539	150	300	48.0 ± 4.6
2453255.515	150	290	36.5 ± 4.5
2453256.555	150	250	27.7 ± 4.5
2453257.534	150	350	21.0 ± 4.4
2453258.492	150	350	16.3 ± 4.4
2453259.531	150	400	3.6 ± 4.4
2453260.536	150	380	-5.3 ± 4.4
2453261.541	150	370	-13.7 ± 4.4
2453262.530	150	400	-21.3 ± 4.4
2453263.536	150	420	-35.7 ± 4.5
2453264.567	150	340	-42.6 ± 4.5
2453264.567	150	340	-42.6 ± 4.5
2453265.490	150	370	-44.8 ± 4.5
2453269.508	150	310	-52.2 ± 4.6
2453271.514	150	310	-44.7 ± 4.5
2453272.540	150	410	-37.5 ± 4.5
2453273.505	150	360	-28.7 ± 4.4

Notes. The second column indicates the exposure time while the third column gives the S/N ratio in the spectrum at ≈5400 Å. The last column gives the RV of the primary star.

Table A.2. Journal of the observations of HR 6819 from the BeSS.

HJD [d]	Time [s]	Resolving power
2455821.045	3400	3000
2456168.065	300	600
2456923.978	100	1000
2457274.066	2400	15 000
2457963.044	1200	15 000
2458335.035	1200	15 000
2458775.957	1200	15 000
2458981.000	1800	15 000

Notes. The second column indicates the exposure time while the third column gives approximate resolving power.

Appendix B: 1999 vs. 2004

We attempted to derive an orbital solution using the 1999 data alone. We assumed $e = 0$ and the same period given in Table 1, and varied the remaining orbital parameters. Doing so, we find that the 1999-data yield slightly different results. We find $K_1 = 54.2 \pm 1.2\,\mathrm{km\,s^{-1}}$ (instead of $60.4 \pm 1.0\,\mathrm{km\,s^{-1}}$). This is probably due to the low number of spectra in 1999 (12 epochs) that cover only half the orbital period.

Similarly, we tried to perform disentangling along the K_2-axis using the 12 observations taken during the 1999 epoch alone (see Sect. 4). The results for the He I lines, Fe I + O II lines, and Balmer lines (excluding Hα for consistency with the 2004 epoch) are shown in Fig. B.1. Evidently, using the 1999 epoch alone, larger values of K_2 are preferred. The Fe and He measurements lie slightly above those of the 2004 measurements (cf. Fig. 5), but well within their respective 1σ errors. The Balmer lines imply a significantly larger K_2 in the 1999 epoch, but the corresponding K_2 values are consistent within 2σ. A weighted average of all measurements for the 1999 epoch yields $K_2 = 8.9 \pm 2.4\,\mathrm{km\,s^{-1}}$. This is significantly larger than the 2004 measurement of $K_2 = 4.0 \pm 0.8\,\mathrm{km\,s^{-1}}$, but consistent within 2σ.

A value of $K_2 \approx 9\,\mathrm{km\,s^{-1}}$ would not change the core of our conclusions, that is that HR 6819 is a binary comprising a stripped primary and a rapidly rotating Be secondary. It would, however, imply a less extreme mass ratio of $M_2/M_1 \approx 7$ and

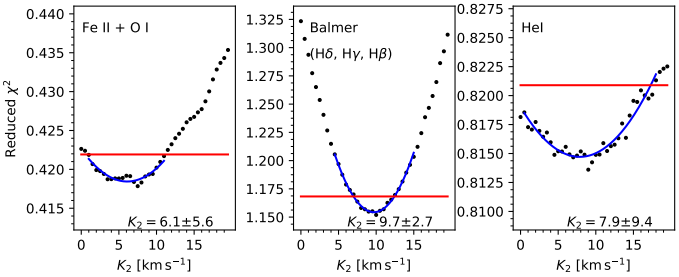

Fig. B.1. Like Fig. 5, but using the 12 spectra of the 1999 epoch instead of the 51 spectra of the 2004 epoch.

a more massive B-type primary with $M_1 \approx 1\,M_\odot$. The short time coverage of the observations and the very strong variability observed during the 1999 epoch may well impact the validity of the results obtained for the 1999 epoch. Regardless, the analysis of the 1999 epoch further illustrates that evidence for a static Be star, as proposed by Rivinius et al. (2020), is lacking.

Appendix C: Are the K_2 measurements significant?

Table C.1. K_2 measurements derived from shift-and-add and Fourier disentangling of individual lines, along with the corresponding values of the reduced χ^2 obtained at minima.

Line	Shift-and-add	Fourier
	K_2 [km s^{-1}]	
Hβ	3.5 ± 1.3	$4.5^{+1.5}_{-2.0}$
Hγ	5.3 ± 2.2	$5.5^{+3.5}_{-3.0}$
Hδ	$3.3^{+4.6}_{-3.3}$	$7.5^{+5.0}_{-7.5}$
Fe II λ4584	4.1 ± 4.0	$3.0^{+4.0}_{-3.0}$
Fe II λ5169	3.5 ± 3.0	4.0 ± 4.0
Fe II λ5198	$3.2^{+5.9}_{-3.2}$	$3.5^{+7.5}_{-3.5}$
Fe II λ5235	8.4 ± 5.0	$6.0^{+8.0}_{-6.0}$
Fe II λ5276	3.8 ± 3.8	$7.0^{+5.0}_{-7.0}$
Fe II λ5317	3.8 ± 2.2	3.0 ± 3.0
Fe II λ5363	$0.5^{+11.1}_{-0.5}$	$9.0^{+7.0}_{-9.0}$
O I λ8446	4.2 ± 2.2	$1.5^{+3.5}_{-1.5}$
He I λ4009	$0.0^{+19.1}$	$0.0^{+10.0}$
He I λ4026	$5.3^{+9.2}_{-5.3}$	$0.0^{+9.5}$
He I λ4122	$13.2^{+13.8}_{-13.2}$	$0.0^{+3.5}$
He I λ4144	$2.5^{+6.9}_{-2.5}$	$0.5^{+12.0}_{-0.5}$
He I λ4388	$4.6^{+8.7}_{-4.6}$	$1.0^{+19.0}_{-1.0}$
He I λ4472	$2.6^{+11.9}_{-2.6}$	$0.0^{+7.5}$
Weighted mean	4.0 ± 0.8	3.7 ± 1.0

Table C.1 gives an overview over the K_2 measurements of individual lines obtained by shift-and-add and the Fourier method. It shows that for Fe II and Balmer lines, both techniques yield similar results. The measurements based on He I lines, however, favour values close to zero in the Fourier technique which is in contrast to the measurements of the shift-and-add technique.

Given the low RV amplitude derived for the Be component using the Balmer and Fe II lines, $K_2 = 4\,\mathrm{km\,s^{-1}}$, an given the

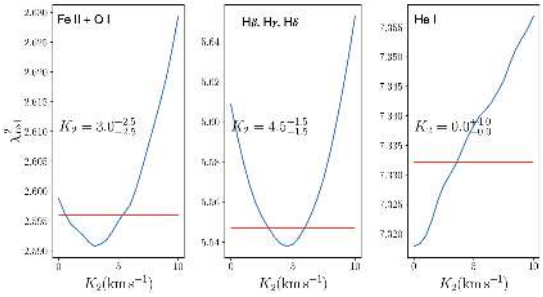

Fig. C.1. Reduced $\chi^2(K_2)$ and corresponding K_2 measurements for individual line groups obtained from the observed data set, but using the Fourier spectral disentangling code `fd3`. The reduced χ^2 is computed in Fourier space and can thus not be directly compared with the one computed by the shift-and-add technique (e.g. Fig. 5).

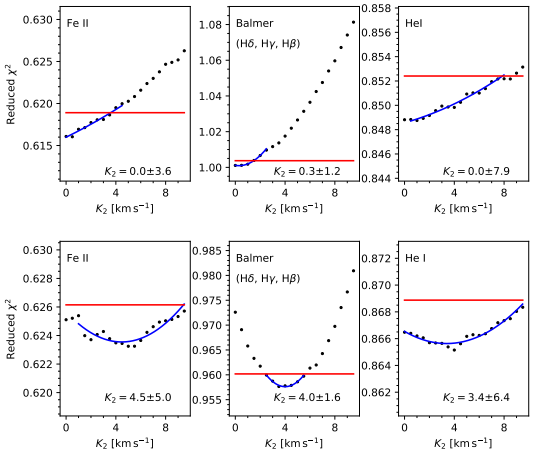

Fig. C.2. Reduced $\chi^2(K_2)$ values obtained for 51 simulated spectra with $K_{2,\mathrm{true}} = 0$ (*top*) and $K_{2,\mathrm{true}} = 4$ (*bottom*), illustrating that the shift-and-add disentangling is successful in retrieving the true K_2 values well within measurement errors.

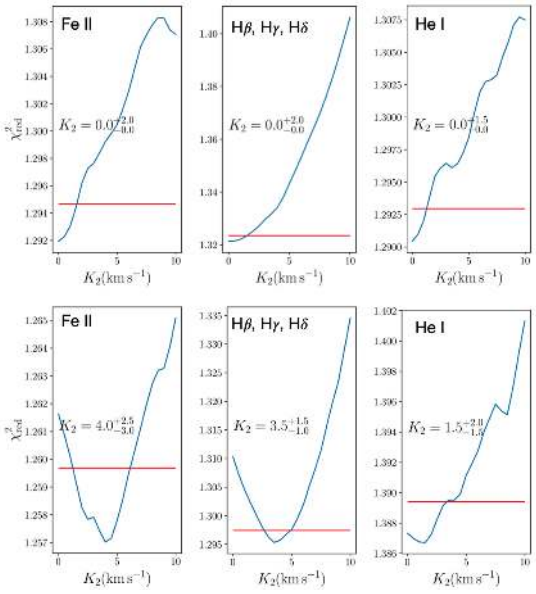

Fig. C.3. Same as Fig. C.2, but using Fourier grid disentangling with `fd3` (*top*: $K_{2,\mathrm{true}} = 0\,\mathrm{km\,s^{-1}}$, *bottom*: $K_{2,\mathrm{true}} = 4\,\mathrm{km\,s^{-1}}$), illustrating the discrepant results obtained using Fourier disentangling in this case. The $K_2 = 4\,\mathrm{km\,s^{-1}}$ semi-amplitude is not unanimously resolved with the Fourier method as it was with the shift-and-add method, even though the reduced chi-squared statistic is of order one.

discrepant results for the He I lines, we investigated the robustness of the disentangling process using artificial data. For this purpose, we created 51 mock spectra of a binary providing the two disentangled spectra as an input, and applying an average S/N comparable to the one in the FEROS data. The mock data mimic the 2004 epoch in terms of their baseline coverage. We fixed the orbital parameters of the primary to those given in Table 1, but performed two different tests for two distinct $K_{2,\mathrm{true}}$ values: $K_{2,\mathrm{true}} = 0\,\mathrm{km\,s^{-1}}$ (static Be) and $K_{2,\mathrm{true}} = 4\,\mathrm{km\,s^{-1}}$ (the result inferred here).

We then performed shift-and-add and Fourier disentangling along the K_2-axis on each of these mock data sets. We used the same lines that were used in our study (see Table C.1). As performed for our analysis, we constructed reduced χ^2 plots for groups of lines, and excluded the Hα line.

The results for the shift-and-add technique are shown in Fig. C.2. Evidently, all three line-groups are successful in retrieving the true $K_{2,\mathrm{true}}$ values well within their respective 1σ errors. The Balmer lines do so most accurately, owing to their high S/N and sharp contrasts. This experiment implies that our results are meaningful. However, we cannot rule out that non-Keplerian variability introduces an additional source of error that is not treated here.

We performed the same experiment with the Fourier disentangling code `fd3` (see Fig. C.3). We find that the Balmer and Fe II lines retrieve the input values of K_2. However, in the $K_{2,\mathrm{true}} = 4\,\mathrm{km\,s^{-1}}$ case, the He I lines yields significantly lower values than the input value. These experiments further show that the He I-based disentangling can hardly be used to distinguish between the cases with $K_{2,\mathrm{true}} = 0$ and $4\,\mathrm{km\,s^{-1}}$ given the large errors and systematic bias observed.

Appendix D: List of potential progenitor systems

Table D.1 lists all systems from the S_{B^9} catalogue that are used on the discussion of the evolutionary scenario of HR 6819 in Sect. 7.2.

Table D.1. Binaries considered from the S_{B^9} catalogue.

Name	q	Period [d]	Reference
		Detached	
HS Her	0.3900	1.637	Khaliullin & Khaliullina (2006)
ζ Phe	0.6491	1.667	Andersen (1983)
VV Ori	0.4503	1.485	Terrell et al. (2007)
IQ Per	0.4932	1.744	Lacy & Frueh (1985)
LT CMa	0.6016	1.760	Bakiş et al. (2010)
IM Mon	0.6062	1.190	Bakis et al. (2011)
μ_1 Sco	0.6451	1.446	van Antwerpen & Moon (2010)
V526 Sgr	0.7400	1.920	Lacy (1997)
CO Lac	0.8228	1.542	Švaříček et al. (2008)
AH Cep	0.8286	1.775	Holmgren et al. (1990)
RX Her	0.8466	1.779	Jeffreys (1980)
V470 Cyg	0.8775	1.874	Russo et al. (1982)
U Oph	0.9027	1.677	Johnston et al. (2019)
V760 Sco	0.9277	1.731	Andersen et al. (1985)
DW Car	0.9389	1.328	Clausen et al. (2007)
AO Mon	0.9487	1.885	Giuricin et al. (1980)
PV Cas	0.9791	1.751	Popper (1987)
FZ Cma	0.9908	1.273	Giuricin & Mardirossian (1981)
		Semi-detached	
V1425 Cyg	1.558	1.252	Değirmenci et al. (1996)
AI Cru	1.635	1.418	Bell et al. (1987)
IU Aur	1.993	1.812	Harries et al. (1998)
V Pup	2.035	1.455	Andersen et al. (1983)
V1898 Cyg	5.210	1.513	Dervisoglu et al. (2011)
		Contact or near-contact	
V606 Cen	0.5270	1.495	Lorenz et al. (1999)
SX Aur	0.5418	1.210	Öztürk et al. (2014)
π Sco	0.6328	1.570	Lefèvre et al. (2009)
SV Cen	0.7075	1.659	Drechsel et al. (1982)
RZ Pyx	0.8211	0.6563	Zhao et al. (2018)
GO Cyg	0.8528	0.7178	Ulaş et al. (2012)
V701 Sco	0.9931	0.7619	Bell & Malcolm (1987)
		Unknown	
HD 23625	0.7193	1.941	
HD 175544	0.7855	1.986	
V599 Aql	0.6244	1.849	
σ Aql	0.7894	1.950	
HD 191566	0.5985	1.818	
7 CrB A	0.9043	1.724	
HD 222900	0.8789	0.6847	

Notes. Mass ratios and periods are taken from the catalogue, while the classification as detached, semi-detached or contact comes from the specified reference.

Appendix E: Setup of MESA simulations

The simulation presented in Sect. 7.2 was computed with version 12778 of the MESA code, using an initial composition of $X = 0.7$, $Y = 0.28$ and $Z = 0.02$ for both stars. For simplicity, we do not include stellar rotation, or tidal coupling in this simulation. Opacities are computed from the OPAL project (Iglesias & Rogers 1996), using solar-scaled metal abundances from Grevesse et al. (1996). We use the OPAL equation of state (Rogers & Nayfonov 2002). Nuclear reaction rates are taken from Angulo et al. (1999) and Cyburt et al. (2010), and we use the 8-isotope network `basic.net` which includes H^1, He^3, He^4, C^{12}, N^{14}, O^{16}, Ne^{20} and Mg^{24} (Paxton et al. 2011). Convective boundaries are determined using the Ledoux criterion, with exponential overshooting given by parameters $f = 0.01$ and $f_0 = 0.005$. Semiconvective mixing is modelled as in Langer et al. (1983) with an efficiency parameter $\alpha_{\mathrm{sc}} = 1$, and thermohaline mixing follows the model of Kippenhahn et al. (1980) with an efficiency parameter $\alpha_{\mathrm{th}} = 1$. We do not include mass loss from stellar winds. Mass transfer due to Roche lobe overflow is computed as in Kolb & Ritter (1990). Although the model experiences a short-lived contact phase during fast Case A mass transfer, for simplicity we ignore this and apply the model of Kolb & Ritter (1990) as if the system remained semi-detached. A complete set of input files to reproduce our simulation will be included upon acceptance of the paper.